Assimilation of L-band InSAR snow depth retrievals for improved snowpack quantification

Prabhakar Shrestha[1] and Ana P. Barros[1]

[1]Department of Civil and Environmental Engineering, University of Urbana-Champaign, Urbana, Illinois, USA.

Corresponding Author: Ana P. Barros (barros@illinois.edu)

Abstract

The integration of snow hydrology models and remote sensing observations via data assimilation is a promising method to capture the dynamics of seasonal snowpacks at high spatial resolution and reduce uncertainty with respect to snow water resources. In this study, we employ ~~a modified~~ interferometric Synthetic Aperture Radar (InSAR) technique to quantify snow depth change using modeled snow density and assimilate the referenced and calibrated retrievals into a multilayer snow hydrology model (MSHM). Although the impact of assimilating snow depth change is local in space and time, the impact on snowpack mass properties (snow depth or SWE) is cumulative, and the InSAR retrievals are valuable to improve snowpack simulation and capture the spatial and temporal variability of snow depth or SWE. Details in the estimation algorithm of InSAR snow depth or SWE changes, referencing and calibration prove to be important to minimize errors during data assimilation.

1 Introduction

Remote sensing and distributed modelling of snowpack with data assimilation is a promising methodology to quantify snow water resources (including condition) and reduce uncertainty. Current and upcoming snow remote sensing using Synthetic Aperture Radar (SAR) aim to provide global coverage at hyper-resolution, which is needed to quantify snow variability with reduced uncertainty. Recent studies have either mostly used backscatter approaches (Lievens et al., 2019, 2022; Singh et al., 2024; Tsang et al., 2021)~~(Lievens et al., 2019, 2022; Singh et al., 2024; Tsang et al., 2021)~~ or interferometric SAR (InSAR) techniques(Guneriussen et al., 2001)~~(Guneriussen et al., 2001)~~ to quantify snow depth and snow water equivalent (SWE). The latter have been applied extensively for SWE retrievals from dry snowpacks using ground-based (e.g. Leinss et al., 2015; Ruiz et al., 2022)~~(e.g. Leinss et al., 2015; Ruiz et al., 2022)~~and satellite-based SARs (e.g. Conde et al., 2019; Dagurov et al., 2020; Deeb et al., 2011; Guneriussen et al., 2001; Lei et al., 2023; H. Li et al., 2016; S. Li & Sturm, 2002; Liu et al., 2017)~~e.g. Conde et al., 2019; Dagurov et al., 2020; Deeb et al., 2011; Guneriussen et al., 2001; Lei et al., 2023; H. Li et al., 2016; S. Li & Sturm, 2002; Liu et al., 2017)~~. The InSAR technique assumes that the volume backscatter and absorption of microwave signal in the snowpack are negligible with the backscatter at the ground-snowpack interface being dominant while ~~refraction~~ slow propagation of radar waves through snowpack (depending on dielectric property) results in phase delay. Previous studies have shown also that the InSAR retrievals are more suitable at longer wavelengths (e.g., L-band), owing to transparency of ==dry snow==, preservation of coherence for longer periods of time and larger threshold for phase wrapping. With the upcoming NASA-ISRO (Indian Space Research Organization) SAR (NISAR) mission, multiple studies with airborne L-band UAVSAR (Uninhabited Aerial

86 Vehicle Synthetic Aperture Radar) data from 2020 NASA SnowEx campaign have

87 already demonstrated the potential of InSAR for snow remote sensing (e.g. Bonnell et

88 al., 2024; Deeb et al., 2021; Hoppinen et al., 2023; Idowu and Marshall, 2022; Marshall

89 et al., 2021; Palomaki and Sproles, 2023; Tarricone et al., 2022)~~(e.g. Bonnell et al.,~~

90 ~~2024; Deeb et al., 2021; Hoppinen et al., 2023; Idowu and Marshall, 2022; Marshall et~~

91 ~~al., 2021; Palomaki and Sproles, 2023; Tarricone et al., 2022)~~.

92   InSAR retrieval algorithms need spatial data of snow density and referencing to

93 estimate the spatial variability in absolute snow depth or snow water equivalent (SWE).

94 Leinss et al. (2015)~~Leinss et al. (2015)~~ have proposed a modified InSAR technique to

95 circumnavigate the need of snow density in SWE retrievals by introducing an additional

96 parameter with very small variability for a range of incidence angles and snow density,

97 their approach also assumes that the vertical profile of snow density does not change

98 between the two dates for each InSAR pair. However, the density profiles can change

99 depending on the time interval between revisits, new snowfall events, and weather

100 conditions that may impact the top layer of the snowpack. Furthermore, snow density

101 might still be needed in referencing the retrievals to obtain absolute snow depth or

102 SWE for assimilation purposes. Hyper-resolution snow hydrology models driven by

103 realistic hydrometeorological forcing can potentially provide a good estimate of ~~snow~~

104 ~~density~~ for the InSAR algorithm, and in turn the assimilation of InSAR retrievals can

105 potentially improve the modeled snowpack states. Earlier studies have already shown

106 the potential of assimilating retrieval of snow depth or SWE from airborne or satellite

107 SAR to improve modeled snowpack and reduce uncertainty (e.g.Girotto et al., 2024;

108 Pflug et al., 2024; Shrestha and Barros, 2024~~Girotto et al., 2024; Pflug et al., 2024;~~

109 ~~Shrestha and Barros, 2024~~).The upcoming launch of the ~~NASA-ISRO SAR (~~NISAR~~)~~

110 mission that will provide L-band measurements globally provides impetus to

111 investigate the assimilation of InSAR retrievals and associated uncertainty

quantification with potential application to operational water prediction. Here, we leverage the multiple in-situ and airborne snow measurements available from NASA's SnowEx'20 (Marshall et al., 2019)~~(Marshall et al., 2019)~~ campaign over Grand Mesa to 1) evaluate L-band InSAR retrievals of snow depth, and 2) assimilate the retrievals into a distributed snow hydrology model to evaluate the impact on the simulated macro-physical snow properties and their uncertainties. We evaluate the L-band InSAR retrievals at their native resolution over different snow depths and land covers against ground-based measurements and airborne Lidar (Light Detection and Ranging) retrievals. The InSAR retrievals with the common first flight date (but different repeat pass) with ~~available observed spatial~~ airborne lidar measurements of snow depth ~~measurements~~ were used for assimilation at different time windows and the other retrievals were used to evaluate the ensemble snow hydrology model prediction of snow properties and to characterize the impact of assimilating the InSAR retrievals of snow depth.

2 Methods

2.1 Study Area

The study area is located over the western part of Grand Mesa plateau, Colorado, USA (GM domain; Fig. 1). The land cover is dominated by grassland and mixed forests across the plateau with elevations ranging from 3000 to 3200 m. There are several scattered open water bodies (e.g., lakes and reservoirs), as well as areas with shrubs and wetlands. During the SnowEx'20 campaign, Grand Mesa was used to host an Intensive Observation Period (IOP) during the snow-on season, including bi-weekly UAVSAR flights and airborne Lidar data collections.

2.2 Data

2.2.1 UAVSAR

UAVSAR is a fully polarimetric L-band synthetic aperture radar designed to obtain high quality airborne repeat pass interferometry (Hensley et al., 2008; Rosen et al., 2006)(Hensley et al., 2008; Rosen et al., 2006). The radar operates at a frequency of 1.26 GHz ($\lambda = 0.2379\,m$) with a bandwidth of 80 MHz, and is mounted on the NASA NASA Gulfstream III, flying at a nominal altitude of 13800 m. UAVSAR data are available from the ASF-DAAC for multiple campaigns (https://api.daac.asf.alaska.edu/services/utils/mission_list). The uavsar_pytools (Keskinen et al., 2022;Keskinen et al., 2022;https://github.com/SnowEx/uavsar_pytools) was used to download and convert InSAR georeferenced binary grid files to geotiffs in WGS84 for Grand Mesa (SnowEx'20). The interferometric data consists of the interferogram, coherence, unwrapped phase in quad polarizations, including the digital elevation and incidence angles along the flight path. In some cases, all polarizations were not available. There were 7 InSAR pairs available based on 5 UAVSAR flights for repeated flight paths at a heading of 274° (Table 1). The interval between the InSAR pairs varied between 7 to 40 days (e.g. track 3-5 (11d), 3-8 (18d), 3-13 (25d),3-17 (40d),5-8 (7d),8-13 (7d) and 13-17 (15d)).

2.2.2 Snow Pit and Snow Pole Measurements

The snow pit data include measurements of snow temperature, snow depth, snow density, snow stratigraphy, snow grain size, liquid water content, and snow water equivalent over Grand Mesa. The SNEX20_GM_SP collection (Vuyovich et al., 2021)(Vuyovich et al., 2021) has 154 snow pit measurements between 27 January and 12 February 2020. Similarly, the SNEX20_TS_SP collection(Mason et al.,

2024)(Mason et al., 2024) has time-series of snow pit measurements between October 2019 and May 2020, obtained by the SnowEx community during the 2020 campaign.

The snow pole data (SNEX20_SD_TLI) consists of snow depth measurements based on time-lapse imagery by capturing a snow pole in each imagery(Breen et al., 2022)(Breen et al., 2022). The temporal coverage for these data is from 29 September 2019 through 10 June 2020. The cameras took either three images daily (11AM, 12 PM, 1PM) or twice daily (11AM and 12PM). The cameras were placed in 9 different environments over the Grand Mesa based on a combination of tree-density map (treeless, sparse and dense) and reference snow depth (shallow, intermediate and deep). The snow depth classification was based ons from Airborne Snow Observatory (ASO) Lidar retrievals fromon 8 Feb 2017 (shallow, intermediate and deep). The error estimates for each camera vary and range from ± 2 to ± 16 cm. More details are also available from https://snow.nasa.gov/sites/default/files/users/user354/SNEX-Campaigns/2020/NASASnowEx20_ExperimentPlan_v15.pdf

2.2.3 ASO

The Airborne Snow Observatory(ASO; Painter et al., 2016)(ASO; Painter et al., 2016) Lidar derived snow depths at 3 m and 50 m resolution for Grand Mesa were available for Feb 1/2 (fused together) and Feb 13 during the SnowEx'20 campaign. The snow depths over forested area represent snow depths at the ground. SWE estimates were also available from ASO at 50 m resolution, based on bias corrected snow density using a snow hydrology model at 50 m resolution. The reported uncertainty in the data was 5.8 cm and 1.7 cm at 3 m resolution for the two dates, and less than 1 cm at 50 m resolution for both dates. In the ASO retrievals for SWE, the snow density was obtained by calibrating the modelled density with ground-based observations.

2.2.4 Atmospheric data

The High-Resolution Rapid Refesh (HRRR; Dowell et al., 2022)~~Dowell et al., 2022)~~ 3 km first hour forecast data for water year 2020, was downloaded using a python package(Blaylock, 2024; ~~(Blaylock, 2024;~~ (https://doi.org/10.5281/zenodo.4567540). The HRRR ensemble consists of 36 members for DA and 9 members for forecast run but were not available in the servers except the single forecast. This HRRR data were used both to estimate atmospheric correction of InSAR phase and as offline atmospheric forcing for the snow hydrology model. The HRRR grids interpolated to regular geographic grids are also outlined in the GM domain (Fig. 1).

2.3 InSAR snow depth retrieval

The total interferometric phase difference obtained with repeat pass SAR data over a snow-covered region includes contributions due to phase impacts from flat Earth, local topography, atmospheric delay, snowpack, and random and systematic errors. While the random error mostly comes from the temporal decorrelation, assuming that phase impacts from flat Earth, local topography and systematic errors are accounted for in the UAVSAR InSAR processing chain, the extraction of the phase contribution only requires accurate estimation of phase contribution due to atmospheric delay (see Appendix A1). With known InSAR phase difference ($\Delta\phi_s$) due to the presence of snowpack, the change in snow depth (Δz_s) can be estimated following Guneriussen et al. (2001)~~Guneriussen et al. (2001)~~ for coherent reflections:

$$\Delta z_s = -\left(\frac{\lambda}{4\pi}\right)\frac{\Delta\phi_s}{(cos\theta_i - \sqrt{\varepsilon - sin^2\theta_i})} \tag{1}$$

where λ is the SAR wavelength, θ_i is the incidence angle and ε is the bulk snowpack permittivity. For dry snow, ε'' is negligible compared to ε' and the relationship

209 between snow density ρ_s [kgm^{-3}] and permittivity can be expressed according to

210 Matzler, (1996) and Wiesmann and Mätzler (1999~~Matzler, (1996) and Wiesmann and~~

211 ~~Mätzler (1999~~) as follows:

$$\varepsilon = 1 + 1.6 * 10^{-3}\rho_s + 1.8 * 10^{-9}\rho_s^3 \qquad (2)$$

213 Field measurements of density data are generally sparse and may not be

214 available for all the periods. Also, for future NISAR mission, field measurements alone

215 will not be able to provide the snow density for all grid locations. So, we use modeled

216 snow density (MSHM reference run) driven by atmospheric forcing from an operational

217 numerical weather prediction (NWP), which can be applied everywhere to obtain the

218 bulk snowpack permittivity.

219 Interferometric coherence is important to assess the uncertainty in the retrievals

220 of snow depth, as the retrieval errors increase with decreases in coherence. Ruiz et al.

221 (2022)~~Ruiz et al. (2022)~~ used a ground based 1-10 GHz SAR system with InSAR

222 capabilities to examine the environmental impact on the observed coherence for snow

223 covered surface. For example, increases in air temperature leading to snow melt are

224 associated with large drops in snow coherence, besides wind, precipitation and large

225 changes in temperature gradients. Compared to X, C and S-band, L-band

226 measurements exhibit higher coherence over longer temporal baselines, and lower

227 error in SWE retrieval, indicating better suitability for InSAR applications.

228 The estimation of Δz_s following Eq. (1) assumes that the density of the snowpack

229 is uniform with depth and that the underlying profile does not change with time. The

230 latter assumption is problematic as the snow density of the underlying profile could

231 change due to physical processes (e.g. compaction) depending on the temporal

232 baseline of the repeat pass and fresh snow. Besides, natural snowpacks are

233 characterized by multi-layer vertical stratigraphy with varying snow density and the

234 phase delay is an integral of the phase delay over the multiple layers (Liens et al.

235 2015). Using $\Delta SWE = \sum_{j=1}^{N} \Delta z_{s,j} \rho_s, j / \rho_w$, where ρ_w is the density of water, and i=1,N

236 are the multiple layers, Liens et al. (2015) proposed a linear relationship between

237 InSAR phase change and SWE change as follows:

238

239 $$\Delta SWE = -\Delta\emptyset_s \left(\frac{\lambda}{2\pi\alpha}\right) \left(1.59 + \theta_i^{\frac{5}{2}}\right)^{-1}$$ 3

240 where α is an optimal correction factor ranging from $0.92 - 1.07$ for a wide range

241 of incidence angles (up to 65°) and snow densities (up to 900 kgm⁻³). With this

242 formulation and using an optimal α, they estimated a maximum error of 10%. To reduce

243 the uncertainty in snow density, the above method could be directly used to estimate

244 changes in SWE. However, errors due to variations in density profile tied to the

245 temporal baseline between the repeat passes remain to be addressed.

246 Since we evaluate the model results with snow depth measurements from the

247 lidar and ground-based measurements, we employ Eq. 1 for the estimation of snow

248 depth change in this study. Earlier studies (e.g. Bonnell et al., 2024; Marshall et al.,

249 2021; Palomaki and Sproles, 2023) have also used the same approach. Also, InSAR

250 retrievals only provide change in snow depth or SWE, so even for SWE changes, one

251 would require prior SWE measurements or snow depth and snow density to obtain

252 absolute SWE for assimilation. In general, snow depth measurements are more readily

253 available (e.g. lidar or ground measurements) and models with data assimilation can

254 provide close estimate of snow density, so this study also provides a framework for

255 using InSAR snow depth change for data assimilation. Using the atmospherically

256 corrected unwrapped phase images from the UAVSAR data, the snow depth was

257 retrieved over the GM domain in the native grid resolution (approx. 5 m) using average

258 bulk snow density between two repeat pass dates from MSHM reference runs. Note

259 that the estimated change in snow depth is also well below the limit for possible phase

260   wrapping effect in L-band, which is around 69 cm for $\lambda = 23.6\ cm,$ ~~and~~ $\theta_i = 23°$ ~~$, \rho =$~~

261   ~~$s. = 300\ kg, m - -3.$~~ and $\rho_s = 300 kgm^{-3}$ (Deeb et al., 2011). ~~(Deeb et al., 2011).~~ Here,

262   it is also important to note that the estimated change in snow depth is a relative change,

263   and without a snow-free scene or known point change in snow depth, it's not possible

264   to relate the relative change in snow depth to absolute snow depth change. Previous

265   studies (e.g. Bonnell et al., 2024; Conde et al., 2019; Hoppinen et al., 2023; Palomaki

266   and Sproles, 2023; Tarricone et al., 2022)~~(e.g. Bonnell et al., 2024; Conde et al., 2019;~~

267   ~~Hoppinen et al., 2023; Palomaki and Sproles, 2023; Tarricone et al., 2022)~~ have used

268   different methods (e.g. finding pixels with no changes or using pixels with known

269   changes) to calibrate the InSAR retrievals to obtain absolute change in snow depth or

270   SWE. In this study we use the snow pole measurements over grasslands for the

271   calibration. For cases, where the measurements cannot be collocated due to missing

272   retrievals, we use the snow pole measurement over the sparsely forested areas. In

273   addition, we use an average over a 3x3 square box in the UAVSAR scene to reduce

274   any uncertainty due to GPS location of snow pole measurements. The InSAR snow

275   depth change for a 3x3 square box (native resolution) was compared with snow pole

276   measurements from treeless environment (W1A, W1B and W3A; linearly interpolated

277   to the time of repeat pass flight) for calibration, and the average value was used for the

278   calibration. For Feb 1-12 retrievals in HV and VH polarization (which had lot of missing

279   data) snow pole measurements from W5A, W6B and W6C were used for calibration.

280   Further, we use VV polarization with higher coherence for spatial evaluation with lidar

281   data, but since it was not available for all retrievals, and HH polarization also exhibit

282   higher coherence and similar results to VV polariztion, HH is used for the InSAR

283   retreivals and data assimilation.

284

2.4 MPDAF and Experiment Setup

The Multi-Physics Data Assimilation Platform (MPDAFv1.0; Shrestha and Barros, 2024)(MPDAFv1.0; Shrestha and Barros, 2024) employs a coupled framework of Multilayer Snow Hydrology Model (MSHMv3.0; Cao and Barros, 2020; Kang and Barros, 2011b, 2011a; Shrestha and Barros, 2024)(MSHMv3.0; Cao and Barros, 2020; Kang and Barros, 2011b, 2011a; Shrestha and Barros, 2024) and the NCAR Data Assimilation Research Testbed (DART; Anderson et al., 2009; DART, 2023; Anderson et al., 2009; DART, 2023). MSHM is a distributed 1D-column model, that solves the mass and energy budgets of the snowpack. Key physical processes of snow hydrology - snow/rain partitioning, snow accumulation, compaction, melting, melt-runoff including snow microstructure evolution are well represented in the model to simulate the macroscopic and microscopic snow properties. The snow microstructure evolution is simulated using a detailed microphysical scheme based on the CROCUS snowpack model (Vionnet et al., 2012). The bottom boundary conditions are kept constant during the cold season assuming frozen soils for snow-on conditions and fixed deep soil temperature. Fresh snow density in this study is based on the parameterization of Hedstrom and Pomeroy (1998) and wet bulb temperature is used as threshold to partition precipitation as rain or snow (Wang et al., 2019). Currently, the rain versus snow partitioning only allows for existence of rain or snow and does not allow for mixed form of rain/snow. More details about the parameterizations can be inferred from the studies mentioned above. Following Cao & Barros (2020)Cao & Barros (2020), the snow albedo is provided externally using the NLDAS Mosaic Land Surface Model L4 v2.0 albedo data (Xia et al., 2012a; Xia et al., 2012b)(Xia et al., 2012a; Xia et al., 2012b).

In DART, we use the Ensemble Adjustment Kalman Filter (EAKF;Anderson,

310 2003~~Anderson, 2003~~) with enhanced spatially varying state space inflation (Anderson,

311 2009; El Gharamti, 2018)~~(Anderson, 2009; El Gharamti, 2018)~~. Assimilation is carried

312 out with observed integrated quantities like total SWE or total snow depth, and the

313 increments are then distributed vertically to the model states (snow depth, snow

314 density and SWE) using a repartition algorithm(Shrestha & Barros, 2024)~~(Shrestha &~~

315 ~~Barros, 2024)~~. ~~Besides, the cutoff radius that determines the region of spatial impact~~

316 ~~of the assimilated variable was set at approximately 100 m (close to the model~~

317 ~~resolution).~~

318   For ensemble Kalman filters, ensemble size fewer than 20-30 can lead to

319 statistical error and larger ensemble size take longer to run with very little benefit. So,

320 30-100 ensemble size is recommended to use with ensemble Kalman filters in DART.

321 In this study, we have only two DART state vectors and use 48 ensemble members

322 which is also constrained by the computational and data storage requirements for

323 hyper-resolution runs. In MSHM, vertically discretized snow depth and SWE are

324 prognostic variables. However, we only use the integrated quantities of these

325 prognostic variables (i.e. total SWE and total snow depth) as state vectors in DART,

326 which are updated by the ensemble filters (e.g. EAKF used here). The ensemble filter

327 assumes a Gaussian relation between the variables in the joint state space prior

328 distribution. First, update increments are computed for each ensemble sample of the

329 observation variable, which is then used to solve for the increments for each state

330 variable. This requires prior cross covariance of each state variable with observation

331 variable along with variance of the observation variable (see Anderson 2003 for

332 details). Then, we use a newly developed repartition algorithm to distribute the

333 increments in the vertical profile with mass conservation (snow density is updated). For

334 bulk or single layer snow hydrology models, such repartioning is not needed. DA

335 directly impacts the top layers of the snowpack where snow is added or removed based

336　on assimilation increments. The lower layers are only impacted by the modeled snow

337　evolution after the assimilation, primarily due to addition of new layers on top or

338　removal of existing snow layers. The localization setups were used such that the

339　observations only impact model grid points where they are located. The goal is to

340　reduce the impact to surrounding grids with different landcover characteristics, and

341　therefore different retrieval uncertainty such as in the case of forested and non-forested

342　grid points. BesidesSo, the cutoff radius that determines the region of spatial impact of

343　the assimilated variable was set at approximately 100 m (close to the model

344　resolution).

345　　　　The snow hydrology model is setup over the GM domain using approximately 90

346　m resolution with 66×165 grid points. The maximum number of snow layers in the

347　model was set to 30. The merged atmospheric forcing data are also interpolated to

348　regular geographic grid and disaggregated to 90 m resolution. Here, no downscaling

349　algorithms are applied to the forcing data and the disaggregation technique applies

350　homogeneous forcing over the subgrid pixels – this also allows us to highlight the

351　impact of hyper-resolution data assimilation.

352　　　　The MSHM reference run (CTRL) was integrated from Oct 1, 2019, to Apr 1, 2020

353　using the default HRRR forcing data. For data assimilation (DA) runs, 48 ensemble

354　members were generated by perturbing the model forcing data. The precipitation is

355　perturbed using multiplicative noise drawn from a uniform distribution U[−0.4, 0.4]. The

356　incoming shortwave and longwave are also perturbed using a multiplicative noise from

357　a uniform distribution U[−0.05, 0.05] and U[−0.1, 0.1] respectively.

358　　　　Figure 2 synthesizes the availability of ASO Lidar retrievals and L-band InSAR

359　retrievals for assimilation and evaluation of model runs. Here, we use part of the data

360　for assimilation and the remainder are used for evaluation. As stated earlier, the L-band

361　InSAR retrievals only provide information about relative changes in snow depth or

362 SWE, which need to be referenced and calibrated to obtain absolute values needed

363 for assimilation. In the context of distributed modelling at a given resolution, this would

364 require a spatial map of snow depth or SWE for referencing. In this study, we use the

365 ASO Lidar snow depth data at 50 m resolution (Feb 1) as a reference and combine

366 them with aggregated InSAR retrievals of snow depth change I1 (Feb 1-12) , I2 (Feb

367 1-19) and I3 (Feb 1-26) at 50 m resolution to obtain the absolute snow depth pattern

368 over the GM domain on Feb 12, 19 and 26 respectively. Two DA experiments are

369 conducted by assimilating total snow depth: 1) ASO Lidar retrieval on Feb 1, and 2)

370 ASO Lidar retrieval on Feb 1 and referenced InSAR retrievals on Feb 12,19 and 26.

371 We reference the InSAR retrievals by aggregating the data to 50 m resolution grid of

372 the ASO Lidar retrievals from Feb 1, which matches the date of the first InSAR pair in

373 both cases. InSAR retrievals of snow depth change on I5 (Feb 12-19), I6 (Feb 19-26)

374 and I7 (Feb 26-Mar12) are reserved for independent evaluation. In both DA

375 experiments, we assign an observational error of 10 % for the snow depth retrievals at

376 50 m resolution, that is consistent with the errors from the InSAR retrievals using the

377 UAVSAR data in this study.

3 Results

3.1 Meteorological Settings

380   The meteorological conditions based on the HRRR forcing data including air

381 temperature, precipitation and wind speed were analysed for the GM domain (2*5

382 HRRR grids at 3 km resolution). These environmental forcings along with temporal

383 baselines are also the source of variability in interferometric coherence and errors in

384 the retrievals. Figure 3 shows the time-series of air temperature, wind speed and

385 precipitation intensity for the month of February including the first two weeks in March

386 for the NW corner of the GM domain. The month of February was generally cold and

387 windy with temperatures dropping below -20 °C, and wind speeds reaching up to 15

388 m/s. The time-series show cooling and warming periods at a weekly time scale, with

389 some days where the air temperature reached above zero. However, the amplitude of

390 cooling decreases gradually from the end of February to mid-March with more frequent

391 warm periods. There were a few snowfall events between Feb 1-12, Feb 19-26 and

392 Feb 26-Mar 12, which varied in intensity along the GM domain.

393 **3.2 Snow Density**

394　A spatial pattern of bulk snow density is required to compute the snowpack

395 permittivity needed for the InSAR retrieval technique. Uncertainty in snow density

396 estimates can lead to errors in snow depth retrieval. Figure 4 shows the snow density

397 distribution for the InSAR pair (Feb 1-12) using the 50 m resolution ASO Lidar data,

398 snow pit data and model estimates using a reference run (CTRL) for the GM domain.

399 Only the snow pit data within GM domain collected within ±1 day of the InSAR flights

400 were used for analysis. All three data sets show compaction of snow between the two

401 dates, but the model simulates slightly higher snow density for both flight dates and

402 underestimates the spatial variance as observed in the snow pit data and ASO Lidar

403 data as expected given the coarse resolution of the HRRR precipitation forcing (i.e.

404 3km). Note that the snow density in ASO Lidar data is also from a model estimate but

405 it was bias corrected (i.e., locally calibrated) using the snow pit data from SnowEX'20

406 campaign. In the 11-day temporal baseline, the average snow density changes by

407 5.6 %, 11 % and 4 % respectively among the lidar, snow pit and model data. Here, we

408 have to note that the snow density change in pit data could also be attributed due to

409 spatial variability besides compaction, which could be contributing to higher

410 differences.

16

411   To examine the error in snow depth retrieval associated with error in density, we

412   used Eq. 1 to retrieve snow depth change for a fixed phase change due to snow. Figure

413   4d shows the variability in InSAR retrieval of snow depth change as a function of

414   incidence angle, for a phase change of -0.17π using the average snow density from

415   ASO Lidar, snow pit and the MSHM CTRL run. The error generally decreases with

416   increasing incidence angle. The synthetic simulation shows that a 10 % error in snow

417   density can lead to approximately 10 % error in snow depth estimates at lower

418   incidence angles, everything else being the same.

419   **3.3 L-band retrieval of snow depth**

420   The temporal baselines for the L-band retrieval range from 7 to 40 days, and the

421   interferometric coherence generally decreased with increasing temporal base lines as

422   expected. For treeless and forested areas, the mean coherence for 7-day temporal

423   baseline (Feb 12-19) was 0.7 ± 0.15 and 0.65 ± 0.18 respectively. Similarly, for the Feb

424   19-26 pair, it was 0.6 ± 0.18 to and 0.5 ± 0.2 respectively. The coherence decreased to

425   0.39 ± 0.16 and 0.36 ± 0.17 for the 40-day temporal baseline. These values are for the

426   HH polarization, as it was available for all dates (see Table 2). The lower coherence

427   for the Feb 19-26 pair compared to Feb 12-19 pair could be attributed to environmental

428   factors, e.g., larger wind speeds, precipitation event, and intermittent warming (see

429   Fig. 3). The forested area exhibits lower coherence than the treeless area suggesting

430   possible higher uncertainty in the retrievals. The above statistics are based on the

431   NLCD landcover data at 30 m resolution, whereas the native resolution of InSAR

432   retrievals from UAVSAR is in the order of 5 m resolution, and the retrievals over forest

433   contain information from snow depth in tree clearings as well.

3.3.1 Evaluation with ASO Lidar data

The InSAR pair of Feb 1-12 with a temporal baseline of 11 days provides the closest concurrent pair with the ASO Lidar retrieval based on Feb1/2 and Feb 13 to compare the snow depth difference at a scale of 3-5 m resolution. Figures 5a-b show the spatial pattern of interferometric coherence and snow depth change at VV polarization. Figure 5c shows the change in snow depth based on ASO Lidar data for the same region. The western part of this GM subdomain is mostly dominated by snow cover over grasslands, while the eastern part contains snow cover in forested areas with relatively lower coherence. Both the Lidar and L-band retrieval capture the wavy roll like pattern due to scouring and drifting of snow over the grasslands shown earlier by Marshall et al. (2021)Marshall et al. (2021) for a smaller area. Over the eastern part of the subdomain, which is dominated by forest, there are significant discrepancies: in regions with no snow depth change in the ASO Lidar data, a decrease in snow depth is observed in the L-band retrieval.

The average coherence values for this subdomain were 0.51, 0.46, 0.39 and 0.39 for VV, HH, HV and VH polarization respectively. Also, the missing retrievals in the radar scene were 8, 11, 36 and 54 % of the area respectively for the different polarizations (see Table 3). The distribution of snow depth change for co-polarization better matches with the ASO Lidar data compared to cross-polarization (Fig. 5d). The average changes in snow depth for the scene were -2.42, -1.13 and -0.1 cm respectively for ASO Lidar and InSAR VV and HH polarizations. The HV and VH polarization show rightward and leftward shifted peaks respectively. The impact of atmospheric correction was minimal for this retrieval. With and without atmospheric correction, the average snow depth change for the InSAR retrieval (VV) were -1.28 cm and -1.13 cm respectively for the scene. The ASO Lidar and InSAR retrieval are in similar resolution but differ in geolocations, so a quantitative spatial comparison which

18

would require spatial interpolation was not used, but we only explore the patterns and frequency distributions within the same extent. For the frequency distribution (Fig. 5d) between ASO and InSAR (VV), we find R=0.97 and RMSE=2.03 cm, and the previous study (Marshall et al. 2021)(Marshall et al. 2021) found R=0.76, RMSE=4.7cm using the near surface field measured density observations in the retrieval.

While the results were similar for other subdomains (not presented here), the L-band retrievals were found to show a general decrease in snow depth in the western most part of GM domain dominated by forest cover, while the Lidar data shows a contrasting increase in snow depth. Thus, the retrievals show higher uncertainty over the forest areas and further evaluation is needed.

3.3.2 Evaluation with snow pole and snow pit time-series data

The snow pole data provide a time-series of snow depth measurements for locations which are treeless or have sparse/dense trees and can be used for comparison with all available InSAR pairs over the GM domain. We use the linearly interpolated snow pole data in time to reference the InSAR retrievals in HH polarization and obtain absolute snow depth for comparison. Figure 6 shows the evaluation of referenced InSAR retrievals with snow pole data for treeless landcover: a-c), sparse trees : d-f), and dense trees : g-m). In most cases, the L-band InSAR retrievals capture the trend in snow depth change very well for different landcover types. The root mean square errors (RMSE) were similar for different landcovers with approximate values of 4-6 cm (which is consistent with earlier findings by Marshall et al. (2021)Marshall et al. (2021) for same InSAR retrieval but different data for evaluation). We also explored the errors in terms of InSAR pairs. The RMSEs of InSAR estimates were 5.0, 4.9, 4.4, 6.2, 7.3 and 4.2 cm respectively for Feb 1-12 (11d), Feb 1-19(18d), Feb 1-26(25d), Feb 12-19(7d), Feb 19-26(7d) and Feb 26-Mar 12(18d) retrievals at the 12 stations. The errors

485   in InSAR retrievals are within 4-8 % of the absolute snow depth.

486   The time-series from snow pits in the north-western part of the GM domain also

487   provide valuable snow depth measurements to evaluate the InSAR estimates. The

488   time-series contains data across treeless and forest areas (Fig. 7). Here, again we use

489   the snow pit measurements to reference the InSAR retrievals and obtain the absolute

490   snow depth. It must be noted that snow pit measurements were carried out at different

491   locations, but within a few meters. Here, we must note that the temporal variability in

492   the snow depth is also partly contributed by the spatial variability due to change in

493   location of pits. The snow depth was slightly higher for the treeless area compared to

494   the forested area, which were within 0.25 km of each other. The InSAR retrievals can

495   capture some of the trends very well, while showing contrasting results for others like

496   for the case of the snow poles. The coherence was within 0.12-0.~~54~~ 67 and 0.~~33~~42-

497   0.79 for the treeless and forested areas, respectively. ~~The forested areas exhibited~~

498   ~~higher coherence for these measurements, and~~ ~~T~~the errors were 2-9 % and 3-31%

499   respectively for treeless and forest areas. Based on the two comparisons of InSAR

500   retrievals against snow pole and snow pit data, the errors are within 10 % for most of

501   the retrievals with few exceptions.

502   **3.4 Data Assimilation and Evaluation**

503   In this section, we explore the impact of assimilating L-band InSAR retrievals on

504   modeled SWE and particularly modeled snow depth. As already discussed in Section

505   2.4, we use two assimilation experiments including an open loop (without assimilation)

506   and a reference run to explore the time evolution of modeled snowpack over Grand

507   Mesa for the accumulation season in the water year 2020. Figure 8 shows the time-

508   series of spatially averaged modeled snow depth from the different runs. The spatial

509   averaging was done for the grids without trees and open water over the GM domain.

510   The dotted lines indicate the total spread of the ensemble runs. The assimilation of the

511   ASO lidar snow depth on Feb 1 shifts the ensembles upwards and reduces the spread

512   for both DA and DAU runs. It shows that the reference run (CTRL) was largely

513   underestimating snow depth. While some of the ensemble members with positive

514   perturbation of precipitation of precipitation were able to capture the actual snow depth,

515   the ensembles with negative perturbation of precipitation underestimated the total

516   snow depth (see the spread in OL run). The assimilation of referenced InSAR retrievals

517   for Feb 12, 19 and 26 (DAU runs) exhibit a small increase in snow depth for the

518   ensemble averages compared to DA runs.

519   The modeled snowpack was also compared with in-situ measurements to assess

520   the impact of data assimilation. The modeled snow depth and SWE at 90 m resolution

521   were compared to snow pit data (IOP and TSD) in locations without trees. The land

522   cover filtered IOP data contained snow depth and SWE from 28 Jan 2020 to 12 Feb

523   2020. Similarly, the land cover filtered TSD contained snow depth from 19 Dec 2019

524   to Apr 17, 2020. There were 68 IOP and 12 TSD snow pit data available for comparison

525   across the GM domain based on the model simulation spatial extent. The RMSE

526   decreased from 35.2 cm to 18.3 cm for snow depth, and for SWE it decreased from

527   8.9 cm to 5.9 cm. The differences in RMSE between DA and DAU runs for these pits

528   were negligible. The modeled snow depth was also compared against snow pole

529   measurements for locations without trees (3 locations, W1A, W1B and W3A) for the

530   entire model simulation period. The RMSE were 17.6, 21.2 and 27.2 cm for the CTRL

531   run, and decreased to 8.1, 21, and 20.8 cm for the DA runs. For DAU runs, the rmse

532   were 8.5, 22.2 and 19.2 cm respectively (see Table 4).

533   The spatial pattern of the modeled snow depth can be evaluated using the

534   reserved InSAR retrievals from Feb 12-19, Feb 19-26 and Feb 26-Mar12 pairs, that

535   were not used for assimilation. Figure 9 shows the spatial pattern of snow depth

change for these repeat pass retrieval dates along with their distribution for the entire GM domain. The estimates are shown for the retrievals and all the model runs. The InSAR data were aggregated to 90 m resolution for comparison. And the grids with open water bodies and tree covers (sparse or dense) were all masked out. Additionally, for the ensemble runs, the spatial maps were obtained by averaging the ensembles, and the distributions are for the averaged ensembles.

The InSAR retrievals for Feb 12-19 and Feb 19-26 exhibit both increase and decreases in snow depth for the GM domain, while the retrievals for Feb 26-Mar 12 show increase in snow depth only (Fig. 9a-c). As expected, the ensemble average for the open loop (OL) run shows spatial variability at the scale of the atmospheric forcing. ~~but~~ The OL run shows similar tendency as InSAR retrievals, except for Feb 12-19 pair, where it shows decrease in snow depth (Fig. 9d-f). While the DA runs improve the total snow depth and SWE, no improvement in the snow depth change is achieved for the Feb 12-19 pair (Fig. 9g). In addition, there are more grids with decrease in snow depth for the remaining two pairs (Fig. 9h-i) compared to the OL run. Note that the DA does increase the modeled spatial variability in snow depth change.

Compared to other model runs, DAU produces best results with positive increase in snow depth change (Fig. 9j-k), also seen in the widening of the distribution in the positive direction (Fig. 9m-n). This is due to the assimilation of InSAR data on Feb 19 and 26. Since there was no assimilation of InSAR data on Mar 12, there is no improvement in the modeled snow depth change for Feb 26-Mar 12 even in DAU runs (Fig. 9i and Fig. 9l). The increase or relatively larger increase in snow depth change for DAU runs (Fig. 9j-~~l~~m) are mostly for the grids where the InSAR data were available for assimilation (Feb 19 and Feb 26). However, the impact of this assimilation appears local in time, and it does produce any significant improvement for the Feb 26-Mar 12 pair compared to DA runs. Despite the data constraints, these results indicate that the

562 assimilation of InSAR estimates has the potential to improve the spatial pattern of

563 modeled snow depth change. Because the snow depth evolution is accumulative,

564 these changes will impact the overall seasonal evolution of the snowpack.

565 **4   Discussion**

566   The hyper-resolution InSAR retrievals resolve the wavy roll like patterns due to

567 scouring and drifting of snow over the grasslands as captured by the ASO lidar data

568 over the grasslands in the NW part of GM domain, also shown earlier by Marshall et

569 al. (2021)Marshall et al. (2021). However, over forested regions, there are

570 disagreements between the lidar and the InSAR estimates with possible uncertainty in

571 both data sets. The average coherence was similar for VV and HH polarization with

572 slightly higher values for VV polarization and lower for HV and VH polarizations. This

573 resulted in higher percentage of missing retrievals in cross-polarizations. The scene-

574 wide average coherence in HH polarization for the 7-day temporal baseline (treeless

575 area) in the GM domain is around 0.6-0.7 which is consistent with values reported by

576 Ruiz et al. (2022)Ruiz et al. (2022). Similarly, the coherence was around 0.5-0.65 for

577 the forested area indicating that the L-band can maintain good coherence over canopy

578 and, with sufficient penetration depending on tree density and canopy architecture, it

579 can be useful in measuring ground snow depth changes. The forested areas generally

580 exhibited lower coherence as expected and the coherence differences between

581 treeless and forested areas were around 14-23% to 8 % for 7-day and 40-day temporal

582 baselines, respectively. Overall, the InSAR retrievals generally compare well with in-

583 situ measurements from snow pole and snow pit over sparse and dense forests. RMSE

584 of the lidar measurements over snow pole site used in the study was also around 7-8

585 cm for the two dates exhibiting good accuracy. So, more data is required for spatial

23

comparison in forested environments to better understand the differences between lidar and InSAR retrievals.

The interferometric coherence across the GM domain generally decreased with increasing temporal baseline (e.g. by 44 % from 7 to 40-day temporal baseline). This indicates that the retrieval uncertainty and retrieval error will increase with larger time between the repeat passes as expected. Since the underlying density of snowpack will also change between the repeat passes, the retrieval error will also increase when using a constant density in Eq. 1. In this study, the depth weighted density averages or the average bulk density between two repeat pass dates from the reference MSHM model runs were used for the InSAR retrievals. The reference runs generally underestimated the total snow depth and SWE compared to the ASO lidar data and snow pit measurements, but the bulk snow density was slightly higher than the snow pit observations during the IOP over Grand Mesa. This indicates that the HRRR forcing used for the study underestimates the snowfall events, besides model uncertainty associated with wind redistribution of snow which is not accounted for. The modelled higher bulk density could again indicate uncertainty in the fresh snow density(Cao and Barros, 2020; Shrestha and Barros, 2024)(Cao and Barros, 2020; Shrestha and Barros, 2024) and compaction parameterization (e.g. Abolafia-Rosenzweig et al., 2024).(e.g. Abolafia-Rosenzweig et al., 2024). The modelled layered snowpack generally shows a two-layer density profile, with an upper layer exhibiting a gradient and near constant density profile in the lower layer. Upon examining density profiles, the difference in snow density profile in the lower layer varied between 1.5-1.8 % (Feb 19-26) and 6-7 % (Feb 1-26) for 7-day and 25-day temporal baseline. This could be still a lower estimate than the actual change in snow density, as shown earlier for 11-day temporal baseline, which was 4 and 11 % for model and snow pit observations. Therefore, the variability in snow density profiles is small for the 7-day base line, and

24

612   it is large for 25-day base line during the accumulation period. Besides the modelled

613   density has its own bias compared to actual snowpack density due to forcing and

614   model structural uncertainty. However, the calibration of the retrievals to obtain

615   absolute snow depth change from the relative snow depth change could also

616   compensate for these errors. Further in-depth studies are needed to better understand

617   the sources of error.

618   Data assimilation of the ASO Lidar snow depth reduces the error and uncertainty

619   in the modeled snow depth. This also reduced the bulk snow density for the ensemble

620   members with lower snow depth (compared to CTRL run) by 4-5 %, as new snow with

621   lower density is added on the top by the repartition algorithm (Shrestha and Barros,

622   2024)(Shrestha and Barros, 2024). These ensemble members (DA; Fig. 9h-i) also

623   exhibited lower or negative snow depth change for Feb 19-26 and Feb 26-Mar 12

624   compared to OL ensembles, which is reflected in the ensemble averages over the GM

625   domain. However, the assimilation of referenced InSAR retrievals (DAU) produces

626   increase in snow depth changes in the ensemble average compared to DA runs. The

627   impact is most apparent in the grids of the GM domain where the data were available

628   for assimilation. This produced the best distribution of snow depth change compared

629   to observations, showing the potential of InSAR retrievals in improving the modeled

630   snowpack. It also demonstrates HRRR underestimation of snowfall between the dates

631   of the InSAR pairs (e.g. between Feb 26 and Mar 12) and it explains the small snow

632   depth differences in the OL runs compared to InSAR retrievals. The OL shows the

633   increase in snow depth due to snowfall just before Mar 12 (see Fig. 3) albeit

634   underestimated as indicated by the difference in magnitude between the InSAR

635   retrievals and the OL snow depth changes. Likewise, the impact of assimilating InSAR

636   retrievals which improves the simulated snow depth changes (as seen for the first two

637   pairs) highlights the need for high temporal resolution of SAR measurements.

5   Conclusion

This study shows that InSAR retrievals are useful to improve the snowpack simulation and capture its spatial and temporal variability. The assimilation of hyper-resolution retrievals of snow depth is equivalent to a downscaling of precipitation forcing with a bias correction. The RMSE of the InSAR retrievals of absolute snow depth change at native resolution compared to snow pole measurements over different land covers were within 4-6 cm, which corresponds to less than 10 % of the absolute snow depth. However, reference snow depth or SWE is essential to obtain absolute snow depth or SWE for assimilation purposes, which poses a challenge in an operational context. In this situation, one would start from snow-free conditions and build up the absolute snow depth from InSAR retrievals using the prior estimates as reference. Accurate calibration of the estimated relative snow depth change, or SWE will be important to minimize retrieval errors. Further work is also essential for InSAR retrievals in forested areas and complex terrains. Future studies are needed to advance a general framework for calibrating InSAR retrievals and obtaining absolute snow depth or SWE for assimilation into the models.

Code availability

The MPDAF v1.0 software with experiment setups is available from https://github.com/mpdaf23/mpdaf.git. MSHM v3.0 used here is documented in Kang and Barros (2011a, 2011b); Cao and Barros (2020) including the updates described in this paper. MEMLS can be downloaded from http://www.iapmw.unibe.ch/research/projects/snowtools/memls.html. The NCAR DART can be downloaded from https://github.com/NCAR/DART.git.

Data availability

The NASA SnowEx 2020 observation data can be downloaded from NASA National Snow and Ice Data Center Distributed Active Archive Center and ASF DAAC. HRRR atmospheric forcing data can be now downloaded from Amazon Web Services (AWS) courtesy of National Oceanic and Atmospheric Administration (NOAA) and the Registry of Open Data on AWS. The NLDAS albedo data can be downloaded from the NASA GES DISC. Model data and software used for visualization is available from https://uofi.box.com/v/InSARmodeldata.

Author contribution

PS and APB conceptualized the study. PS designed the study, processed the data, conducted the model simulation with data assimilation, carried out the analysis, and wrote the paper. APB acquired the grant for the study and contributed to editing of the manuscript.

Competing interests

The authors declare that they have no conflict of interest.

Acknowledgements

References

Abolafia-Rosenzweig, R., He, C., Chen, F., and Barlage, M.: Evaluating and enhancing snow compaction process in the Noah-MP land surface model, J Adv Model Earth Syst, 16, e2023MS003869, 2024.

Anderson, J.: Spatially and temporally varying adaptive covariance inflation for ensemble filters, Tellus A: Dynamic meteorology and oceanography, 61, 72–83, 2009.

Anderson, J., Hoar, T., Raeder, K., Liu, H., Collins, N., Torn, R., and Avellano, A.: The data assimilation research testbed: A community facility, Bull Am Meteorol Soc, 90, 1283–1296, 2009.

Anderson, J. L.: A local least squares framework for ensemble filtering, Mon Weather Rev, 131, 634–642, 2003.

Blaylock, B. K.: Herbie: Retrieve Numerical Weather Prediction Model Data, https://doi.org/10.5281/zenodo.13329302, August 2024.

Bonnell, R., McGrath, D., Tarricone, J., Marshall, H.-P., Bump, E., Duncan, C., Kampf, S., Lou, Y., Olsen-Mikitowicz, A., and Sears, M.: Evaluating L-band InSAR Snow Water Equivalent Retrievals with Repeat Ground-Penetrating Radar and Terrestrial Lidar Surveys in Northern Colorado, EGUsphere, 2024, 1–33, 2024.

Breen, C. M., Hiemstra, C., Vuyovich, C. M., and Mason, M.: SnowEx20 Grand Mesa Snow Depth from Snow Pole Time-Lapse Imagery, Version 1, Boulder, Colorado USA, 2022.

Cao, Y. and Barros, A. P.: Weather-dependent nonlinear microwave behavior of seasonal high-elevation snowpacks, Remote Sens (Basel), 12, 3422, 2020.

Conde, V., Nico, G., Mateus, P., Catalão, J., Kontu, A., and Gritsevich, M.: On the estimation of temporal changes of snow water equivalent by spaceborne SAR interferometry: a new application for the Sentinel-1 mission, Journal of Hydrology and

Hydromechanics, 67, 93–100, 2019.

Dagurov, P. N., Chimitdorzhiev, T. N., Dmitriev, A. V, and Dobrynin, S. I.: Estimation of snow water equivalent from L-band radar interferometry: simulation and experiment, Int J Remote Sens, 41, 9328–9359, 2020.

DART: The data assimilation research testbed (version 10.7.3), Boulder, Coloardo, 2023.

Deeb, E., Forster, R., Vuyovich, C., Elder, K., Hiemstra, C., and Lund, J.: L-band InSAR depth retrieval during the NASA SnowEx 2020 campaign: Grand mesa, Colorado, in: 2021 IEEE International Geoscience and Remote Sensing Symposium IGARSS, 625–627, 2021.

Deeb, E. J., Forster, R. R., and Kane, D. L.: Monitoring snowpack evolution using interferometric synthetic aperture radar on the North Slope of Alaska, USA, Int J Remote Sens, 32, 3985–4003, 2011.

Dowell, D. C., Alexander, C. R., James, E. P., Weygandt, S. S., Benjamin, S. G., Manikin, G. S., Blake, B. T., Brown, J. M., Olson, J. B., and Hu, M.: The High-Resolution Rapid Refresh (HRRR): An hourly updating convection-allowing forecast model. Part I: Motivation and system description, Weather Forecast, 37, 1371–1395, 2022.

El Gharamti, M.: Enhanced adaptive inflation algorithm for ensemble filters, Mon Weather Rev, 146, 623–640, 2018.

Girotto, M., Formetta, G., Azimi, S., Bachand, C., Cowherd, M., De Lannoy, G., Lievens, H., Modanesi, S., Raleigh, M. S., and Rigon, R.: Identifying snowfall elevation patterns by assimilating satellite-based snow depth retrievals, Science of The Total Environment, 906, 167312, 2024.

Guneriussen, T., Hogda, K. A., Johnsen, H., and Lauknes, I.: InSAR for estimation of changes in snow water equivalent of dry snow, IEEE Transactions on Geoscience and Remote Sensing, 39, 2101–2108, 2001.

Hanssen, R. F.: Radar interferometry: data interpretation and error analysis, Springer Science & Business Media, 2001.

Hensley, S., Wheeler, K., Sadowy, G., Jones, C., Shaffer, S., Zebker, H., Miller, T., Heavey, B., Chuang, E., and Chao, R.: The UAVSAR instrument: Description and first results, in: 2008 IEEE Radar Conference, 1–6, 2008.

Hoppinen, Z. M., Oveisgharan, S., Marshall, H.-P., Mower, R., Elder, K., and Vuyovich, C.: Snow Water Equivalent Retrieval Over Idaho, Part B: Using L-band UAVSAR Repeat-Pass Interferometry, The Cryosphere Discussions, 2023, 1–24, 2023.

Idowu, A. N. and Marshall, H.-P.: Snow depth retrieval from L-band data based on repeat pass InSAR techniques, in: IGARSS 2022-2022 IEEE International Geoscience and Remote Sensing Symposium, 4248–4251, 2022.

Kang, D. H. and Barros, A. P.: Observing system simulation of snow microwave emissions over data sparse regions—Part I: Single layer physics, IEEE transactions on geoscience and remote sensing, 50, 1785–1805, 2011a.

Kang, D. H. and Barros, A. P.: Observing system simulation of snow microwave emissions over data sparse regions—Part II: Multilayer physics, IEEE transactions on geoscience and remote sensing, 50, 1806–1820, 2011b.

Keskinen, Z., Tarricone, J., Surfix, and Marshall, H.: SnowEx/uavsar_pytools: v0.2.0, https://doi.org/10.5281/zenodo.6578193, May 2022.

Lei, Y., Shi, J., Liang, C., Werner, C., and Siqueira, P.: Snow Water Equivalent Retrieval Using Spaceborne Repeat-Pass L-Band SAR Interferometry Over Sparse Vegetation Covered Regions, in: IGARSS 2023-2023 IEEE International Geoscience and Remote Sensing Symposium, 852–855, 2023.

Leinss, S., Wiesmann, A., Lemmetyinen, J., and Hajnsek, I.: Snow water equivalent of dry snow measured by differential interferometry, IEEE J Sel Top Appl

Earth Obs Remote Sens, 8, 3773–3790, 2015.

Li, H., Xiao, P., Feng, X., He, G., and Wang, Z.: Monitoring snow depth and its change using repeat-pass interferometric SAR in Manas River Basin, in: 2016 IEEE International Geoscience and Remote Sensing Symposium (IGARSS), 4936–4939, 2016.

Li, S. and Sturm, M.: Patterns of wind-drifted snow on the Alaskan arctic slope, detected with ERS-1 interferometric SAR, Journal of Glaciology, 48, 495–504, 2002.

Lievens, H., Demuzere, M., Marshall, H.-P., Reichle, R. H., Brucker, L., Brangers, I., de Rosnay, P., Dumont, M., Girotto, M., and Immerzeel, W. W.: Snow depth variability in the Northern Hemisphere mountains observed from space, Nat Commun, 10, 4629, 2019.

Lievens, H., Brangers, I., Marshall, H.-P., Jonas, T., Olefs, M., and De Lannoy, G.: Sentinel-1 snow depth retrieval at sub-kilometer resolution over the European Alps, Cryosphere, 16, 159–177, 2022.

Liu, Y., Li, L., Yang, J., Chen, X., and Hao, J.: Estimating snow depth using multi-source data fusion based on the D-InSAR method and 3DVAR fusion algorithm, Remote Sens (Basel), 9, 1195, 2017.

Marshall, H. , V. C. , H. C. , B. L. , E. K. , D. J. , and N. J.: NASA SnowEx 2020 Experiment Plan, 2019.

Marshall, H.-P., Deeb, E., Forster, R., Vuyovich, C., Elder, K., Hiemstra, C., and Lund, J.: L-band InSAR depth retrieval during the NASA SnowEx 2020 campaign: Grand mesa, Colorado, in: 2021 IEEE International Geoscience and Remote Sensing Symposium IGARSS, 625–627, 2021.

Mason, M., Marshall, H., McCormick, M., Craaybeek, D., Elder, K., and Vuyovich, C. M.: SnowEx20 Time Series Snow Pit Measurements, Version 2, Boulder, Colorado USA, 2024.

Matzler, C.: Microwave permittivity of dry snow, IEEE Transactions on Geoscience and Remote Sensing, 34, 573–581, 1996.

Painter, T. H., Berisford, D. F., Boardman, J. W., Bormann, K. J., Deems, J. S., Gehrke, F., Hedrick, A., Joyce, M., Laidlaw, R., and Marks, D.: The Airborne Snow Observatory: Fusion of scanning lidar, imaging spectrometer, and physically-based modeling for mapping snow water equivalent and snow albedo, Remote Sens Environ, 184, 139–152, 2016.

Palomaki, R. T. and Sproles, E. A.: Assessment of L-band InSAR snow estimation techniques over a shallow, heterogeneous prairie snowpack, Remote Sens Environ, 296, 113744, 2023.

Pflug, J. M., Wrzesien, M. L., Kumar, S. V, Cho, E., Arsenault, K. R., Houser, P. R., and Vuyovich, C. M.: Extending the utility of space-borne snow water equivalent observations over vegetated areas with data assimilation, Hydrol Earth Syst Sci, 28, 631–648, 2024.

Rosen, P. A., Hensley, S., Wheeler, K., Sadowy, G., Miller, T., Shaffer, S., Muellerschoen, R., Jones, C., Zebker, H., and Madsen, S.: UAVSAR: A new NASA airborne SAR system for science and technology research, in: 2006 IEEE conference on radar, 8-pp, 2006.

Ruiz, J. J., Lemmetyinen, J., Kontu, A., Tarvainen, R., Vehmas, R., Pulliainen, J., and Praks, J.: Investigation of environmental effects on coherence loss in SAR interferometry for snow water equivalent retrieval, IEEE Transactions on Geoscience and Remote Sensing, 60, 1–15, 2022.

Shrestha P. and A . P. Barros: Multi-physics Data Assimilation Framework for Remotely Sensed Snowpacks to Improve Water Prediction, Water Resource Research, 2024.

Singh, S., Durand, M., Kim, E., and Barros, A. P.: Bayesian physical–statistical

retrieval of snow water equivalent and snow depth from X-and Ku-band synthetic aperture radar–demonstration using airborne SnowSAr in SnowEx'17, Cryosphere, 18, 747–773, 2024.

Smith, E. K. and Weintraub, S.: The constants in the equation for atmospheric refractive index at radio frequencies, Proceedings of the IRE, 41, 1035–1037, 1953.

Tarricone, J., Webb, R. W., Marshall, H.-P., Nolin, A. W., and Meyer, F. J.: Estimating snow accumulation and ablation with L-band InSAR, The Cryosphere Discussions, 2022, 1–33, 2022.

Tsang, L., Durand, M., Derksen, C., Barros, A. P., Kang, D.-H., Lievens, H., Marshall, H.-P., Zhu, J., Johnson, J., and King, J.: Global monitoring of snow water equivalent using high frequency radar remote sensing, The Cryosphere Discussions, 2021, 1–57, 2021.

Vuyovich, C., H.P. Marshall, K. Elder, C. Hiemstra, L. Brucker, and M. McCormick: SnowEx20 Grand Mesa Intensive Observation Period Snow Pit Measurements, Version 1, NASA National Snow and Ice Data Center Distributed Active Archive Center, 2021.

Wang, X., Zeng, Q., and Jiao, J.: Utilization of WRF 3D Meteorological Data to Calculate Slant Total Delay for InSAR Atmospheric Correction, Remote Sens Earth Syst Sci, 4, 30–43, 2021.

Wiesmann, A. and Mätzler, C.: Microwave emission model of layered snowpacks, Remote Sens Environ, 70, 307–316, 1999.

Xia, Y., Mitchell, K., Ek, M., Cosgrove, B., Sheffield, J., Luo, L., Alonge, C., Wei, H., Meng, J., and Livneh, B.: Continental-scale water and energy flux analysis and validation for North American Land Data Assimilation System project phase 2 (NLDAS-2): 2. Validation of model-simulated streamflow, Journal of Geophysical Research: Atmospheres, 117, 2012a.

Xia, Y., Mitchell, K., Ek, M., Sheffield, J., Cosgrove, B., Wood, E., Luo, L., Alonge, C., Wei, H., and Meng, J.: Continental-scale water and energy flux analysis and validation for the North American Land Data Assimilation System project phase 2 (NLDAS-2): 1. Intercomparison and application of model products, Journal of Geophysical Research: Atmospheres, 117, 2012b.

Abolafia-Rosenzweig, R., He, C., Chen, F., and Barlage, M.: Evaluating and enhancing snow compaction process in the Noah-MP land surface model, J Adv Model Earth Syst, 16, e2023MS003869, 2024.

Anderson, J.: Spatially and temporally varying adaptive covariance inflation for ensemble filters, Tellus A: Dynamic meteorology and oceanography, 61, 72–83, 2009.

Anderson, J., Hoar, T., Raeder, K., Liu, H., Collins, N., Torn, R., and Avellano, A.: The data assimilation research testbed: A community facility, Bull Am Meteorol Soc, 90, 1283–1296, 2009.

Anderson, J. L.: A local least squares framework for ensemble filtering, Mon Weather Rev, 131, 634–642, 2003.

Blaylock, B. K.: Herbie: Retrieve Numerical Weather Prediction Model Data, https://doi.org/10.5281/zenodo.13329302, August 2024.

Bonnell, R., McGrath, D., Tarricone, J., Marshall, H. P., Bump, E., Duncan, C., Kampf, S., Lou, Y., Olsen-Mikitowicz, A., and Sears, M.: Evaluating L-band InSAR Snow Water Equivalent Retrievals with Repeat Ground-Penetrating Radar and Terrestrial Lidar Surveys in Northern Colorado, EGUsphere, 2024, 1–33, 2024.

Breen, C. M., Hiemstra, C., Vuyovich, C. M., and Mason, M.: SnowEx20 Grand Mesa Snow Depth from Snow Pole Time-Lapse Imagery, Version 1, Boulder, Colorado USA, 2022.

Cao, Y. and Barros, A. P.: Weather-dependent nonlinear microwave behavior of seasonal high-elevation snowpacks, Remote Sens (Basel), 12, 3422, 2020.

Conde, V., Nico, G., Mateus, P., Catalão, J., Kontu, A., and Gritsevich, M.: On the estimation of temporal changes of snow water equivalent by spaceborne SAR interferometry: a new application for the Sentinel-1 mission, Journal of Hydrology and Hydromechanics, 67, 93–100, 2019.

Dagurov, P. N., Chimitdorzhiev, T. N., Dmitriev, A. V, and Dobrynin, S. I.: Estimation of snow water equivalent from L-band radar interferometry: simulation and experiment, Int J Remote Sens, 41, 9328–9359, 2020.

DART: The data assimilation research testbed (version 10.7.3), Boulder, Coloardo, 2023.

Deeb, E., Forster, R., Vuyovich, C., Elder, K., Hiemstra, C., and Lund, J.: L-band InSAR depth retrieval during the NASA SnowEx 2020 campaign: Grand mesa, Colorado, in: 2021 IEEE International Geoscience and Remote Sensing Symposium IGARSS, 625–627, 2021.

Deeb, E. J., Forster, R. R., and Kane, D. L.: Monitoring snowpack evolution using interferometric synthetic aperture radar on the North Slope of Alaska, USA, Int J Remote Sens, 32, 3985–4003, 2011.

Dowell, D. C., Alexander, C. R., James, E. P., Weygandt, S. S., Benjamin, S. G., Manikin, G. S., Blake, B. T., Brown, J. M., Olson, J. B., and Hu, M.: The High-Resolution Rapid Refresh (HRRR): An hourly updating convection-allowing forecast model. Part I: Motivation and system description, Weather Forecast, 37, 1371–1395, 2022.

El Gharamti, M.: Enhanced adaptive inflation algorithm for ensemble filters, Mon Weather Rev, 146, 623–640, 2018.

Girotto, M., Formetta, G., Azimi, S., Bachand, C., Cowherd, M., De Lannoy, G., Lievens, H., Modanesi, S., Raleigh, M. S., and Rigon, R.: Identifying snowfall elevation patterns by assimilating satellite-based snow depth retrievals, Science of The Total Environment, 906, 167312, 2024.

36

908 Guneriussen, T., Hogda, K. A., Johnsen, H., and Lauknes, I.: InSAR for estimation
909 of changes in snow water equivalent of dry snow, IEEE Transactions on Geoscience
910 and Remote Sensing, 39, 2101–2108, 2001.

911 Hanssen, R. F.: Radar interferometry: data interpretation and error analysis,
912 Springer Science & Business Media, 2001.

913 Hensley, S., Wheeler, K., Sadowy, G., Jones, C., Shaffer, S., Zebker, H., Miller,
914 T., Heavey, B., Chuang, E., and Chao, R.: The UAVSAR instrument: Description and
915 first results, in: 2008 IEEE Radar Conference, 1–6, 2008.

916 Hoppinen, Z. M., Oveisgharan, S., Marshall, H.-P., Mower, R., Elder, K., and
917 Vuyovich, C.: Snow Water Equivalent Retrieval Over Idaho, Part B: Using L-band
918 UAVSAR Repeat-Pass Interferometry, The Cryosphere Discussions, 2023, 1–24,
919 2023.

920 Idowu, A. N. and Marshall, H. P.: Snow depth retrieval from L-band data based
921 on repeat pass InSAR techniques, in: IGARSS 2022-2022 IEEE International
922 Geoscience and Remote Sensing Symposium, 4248–4251, 2022.

923 Kang, D. H. and Barros, A. P.: Observing system simulation of snow microwave
924 emissions over data sparse regions—Part I: Single layer physics, IEEE transactions
925 on geoscience and remote sensing, 50, 1785–1805, 2011a.

926 Kang, D. H. and Barros, A. P.: Observing system simulation of snow microwave
927 emissions over data sparse regions—Part II: Multilayer physics, IEEE transactions on
928 geoscience and remote sensing, 50, 1806–1820, 2011b.

929 Keskinen, Z., Tarricone, J., Surfix, and Marshall, H.: SnowEx/uavsar_pytools:
930 v0.2.0, https://doi.org/10.5281/zenodo.6578193, May 2022.

931 Lei, Y., Shi, J., Liang, C., Werner, C., and Siqueira, P.: Snow Water Equivalent
932 Retrieval Using Spaceborne Repeat-Pass L-Band SAR Interferometry Over Sparse
933 Vegetation Covered Regions, in: IGARSS 2023-2023 IEEE International Geoscience

and Remote Sensing Symposium, 852–855, 2023.

Leinss, S., Wiesmann, A., Lemmetyinen, J., and Hajnsek, I.: Snow water equivalent of dry snow measured by differential interferometry, IEEE J Sel Top Appl Earth Obs Remote Sens, 8, 3773–3790, 2015.

Li, H., Xiao, P., Feng, X., He, G., and Wang, Z.: Monitoring snow depth and its change using repeat-pass interferometric SAR in Manas River Basin, in: 2016 IEEE International Geoscience and Remote Sensing Symposium (IGARSS), 4936–4939, 2016.

Li, S. and Sturm, M.: Patterns of wind-drifted snow on the Alaskan arctic slope, detected with ERS-1 interferometric SAR, Journal of Glaciology, 48, 495–504, 2002.

Lievens, H., Demuzere, M., Marshall, H.-P., Reichle, R. H., Brucker, L., Brangers, I., de Rosnay, P., Dumont, M., Girotto, M., and Immerzeel, W. W.: Snow depth variability in the Northern Hemisphere mountains observed from space, Nat Commun, 10, 4629, 2019.

Lievens, H., Brangers, I., Marshall, H.-P., Jonas, T., Olefs, M., and De Lannoy, G.: Sentinel-1 snow depth retrieval at sub-kilometer resolution over the European Alps, Cryosphere, 16, 159–177, 2022.

Liu, Y., Li, L., Yang, J., Chen, X., and Hao, J.: Estimating snow depth using multi-source data fusion based on the D-InSAR method and 3DVAR fusion algorithm, Remote Sens (Basel), 9, 1195, 2017.

Marshall, H. , V. C. , H. C. , B. L. , E. K. , D. J. , and N. J.: NASA SnowEx 2020 Experiment Plan, 2019.

Marshall, H.-P., Deeb, E., Forster, R., Vuyovich, C., Elder, K., Hiemstra, C., and Lund, J.: L-band InSAR depth retrieval during the NASA SnowEx 2020 campaign: Grand mesa, Colorado, in: 2021 IEEE International Geoscience and Remote Sensing Symposium IGARSS, 625–627, 2021.

Mason, M., Marshall, H., McCormick, M., Craaybeek, D., Elder, K., and Vuyovich, C. M.: SnowEx20 Time Series Snow Pit Measurements, Version 2, Boulder, Colorado USA, 2024.

Matzler, C.: Microwave permittivity of dry snow, IEEE Transactions on Geoscience and Remote Sensing, 34, 573–581, 1996.

Painter, T. H., Berisford, D. F., Boardman, J. W., Bormann, K. J., Deems, J. S., Gehrke, F., Hedrick, A., Joyce, M., Laidlaw, R., and Marks, D.: The Airborne Snow Observatory: Fusion of scanning lidar, imaging spectrometer, and physically-based modeling for mapping snow water equivalent and snow albedo, Remote Sens Environ, 184, 139–152, 2016.

Palomaki, R. T. and Sproles, E. A.: Assessment of L-band InSAR snow estimation techniques over a shallow, heterogeneous prairie snowpack, Remote Sens Environ, 296, 113744, 2023.

Pflug, J. M., Wrzesien, M. L., Kumar, S. V, Cho, E., Arsenault, K. R., Houser, P. R., and Vuyovich, C. M.: Extending the utility of space-borne snow water equivalent observations over vegetated areas with data assimilation, Hydrol Earth Syst Sci, 28, 631–648, 2024.

Rosen, P. A., Hensley, S., Wheeler, K., Sadowy, G., Miller, T., Shaffer, S., Muellerschoen, R., Jones, C., Zebker, H., and Madsen, S.: UAVSAR: A new NASA airborne SAR system for science and technology research, in: 2006 IEEE conference on radar, 8-pp, 2006.

Ruiz, J. J., Lemmetyinen, J., Kontu, A., Tarvainen, R., Vehmas, R., Pulliainen, J., and Praks, J.: Investigation of environmental effects on coherence loss in SAR interferometry for snow water equivalent retrieval, IEEE Transactions on Geoscience and Remote Sensing, 60, 1–15, 2022.

Shrestha P. and A . P. Barros: Multi-physics Data Assimilation Framework for

Remotely Sensed Snowpacks to Improve Water Prediction, Water Resource Research, 2024.

Singh, S., Durand, M., Kim, E., and Barros, A. P.: Bayesian physical-statistical retrieval of snow water equivalent and snow depth from X-and Ku-band synthetic aperture radar-demonstration using airborne SnowSAr in SnowEx'17, Cryosphere, 18, 747–773, 2024.

Smith, E. K. and Weintraub, S.: The constants in the equation for atmospheric refractive index at radio frequencies, Proceedings of the IRE, 41, 1035–1037, 1953.

Tarricone, J., Webb, R. W., Marshall, H. P., Nolin, A. W., and Meyer, F. J.: Estimating snow accumulation and ablation with L-band InSAR, The Cryosphere Discussions, 2022, 1–33, 2022.

Tsang, L., Durand, M., Derksen, C., Barros, A. P., Kang, D.-H., Lievens, H., Marshall, H.-P., Zhu, J., Johnson, J., and King, J.: Global monitoring of snow water equivalent using high frequency radar remote sensing, The Cryosphere Discussions, 2021, 1–57, 2021.

Vuyovich, C., H.P. Marshall, K. Elder, C. Hiemstra, L. Brucker, and M. McCormick: SnowEx20 Grand Mesa Intensive Observation Period Snow Pit Measurements, Version 1, NASA National Snow and Ice Data Center Distributed Active Archive Center, 2021.

Wang, X., Zeng, Q., and Jiao, J.: Utilization of WRF 3D Meteorological Data to Calculate Slant Total Delay for InSAR Atmospheric Correction, Remote Sens Earth Syst Sci, 4, 30–43, 2021.

Wiesmann, A. and Mätzler, C.: Microwave emission model of layered snowpacks, Remote Sens Environ, 70, 307–316, 1999.

Xia, Y., Mitchell, K., Ek, M., Cosgrove, B., Sheffield, J., Luo, L., Alonge, C., Wei, H., Meng, J., and Livneh, B.: Continental-scale water and energy flux analysis and

validation for North American Land Data Assimilation System project phase 2 (NLDAS-2): 2. Validation of model-simulated streamflow, Journal of Geophysical Research: Atmospheres, 117, 2012a.

Xia, Y., Mitchell, K., Ek, M., Sheffield, J., Cosgrove, B., Wood, E., Luo, L., Alonge, C., Wei, H., and Meng, J.: Continental-scale water and energy flux analysis and validation for the North American Land Data Assimilation System project phase 2 (NLDAS-2): 1. Intercomparison and application of model products, Journal of Geophysical Research: Atmospheres, 117, 2012b.

Appendix A1

The atmospheric delay experienced by a microwave signal can be estimated by integrating the atmospheric refractivity along the line of sight from the surface to the airborne sensor height. Neglecting the impact of ionosphere for the UAVSAR flying at a height of z_s, the scaled up atmospheric refractivity of moist air [N=(n-1)10^6], where n is the refractive index, is given by

$$N(x,z) = k_1 \frac{P}{T} + (k_2 - k_1)\frac{e}{T} + k_3 \frac{e}{T^2} + k_4 W_{cl}$$

where P is pressure [hPa], T is air temperature [K], e is vapor pressure [hPa], W_{cl} is liquid water content [kgm^{-3}], n_e is ionization and f is frequency. The remaining term are constants: $k_1 = 0.776\,KPa^{-1}$, $k_2 = 0.716\,KPa^{-1}$, $k_3 = 3750\,K^2Pa^{-1}$, $k_4 = 1430\,m^3kg^{-1}$. Based on the works of Smith and Weintraub (1953)Smith and Weintraub (1953), the above relation is restricted to certain limits of the variables for an accuracy of 0.5 percent in N(x,z). The limits in this case restrict its use to temperatures of -50 to + 40° C, total pressures of 200 to 1100 mb, water-vapor partial pressures of 0 to 30 mb, and a frequency range of 0 to 30 GHz.

$N(x,z)$ can be further decomposed into the mean and turbulent part for a radar scene as:

$$N(x,z) = \overline{N}(z) + N'(x,z)$$

where $\overline{N}(z)$ is the average vertical stratification for the given resolution of the atmospheric model (here 3 km) and $N'(x,z)$ is the deviation from the average profile along the location x in the radar scene (within the atmospheric grid). Neglecting the turbulent terms, zenith delay L for the mean part can be computed as

$$L = \int_{z_{ref}}^{z_s} \left(k_1 \frac{P}{T} + (k_2 - k_1)\frac{e}{T} + k_3 \frac{e}{T^2}\right) dz$$

Using $dP = -\rho g dz$ and $\rho = P/R_d T$, where ρ is air density [kgm^{-3}] , $R_d =$

42

$287.053 \, Jkg^{-1}K^{-1}$ is the dry gas constant, ang g is acceleration due to gravity, we obtain:

$$L = -10^{-6}\left(k_1 \frac{R_d}{g}\left(P(z_s) - P(z_{ref})\right)\right) + 10^{-6}\int_{z_{ref}}^{z_s}\left((k_2 - k_1)\frac{e}{T} + k_3 \frac{e}{T^2}\right)dz$$

The first term of the right side is the hydrostatic correction term, and the second term is the wet correction term. The atmospheric phase delay along the line of sight (LOS) can then be estimated using the microwave wavelength (λ) and incidence angle (θ_{inc}) as:

$$\emptyset_{atm} = \frac{4\pi}{\lambda}\frac{L}{\cos(\theta_{inc})}$$

The above simple approximation for computing atmospheric phase delay along the LOS could introduce additional uncertainty(Wang et al., 2021)(Wang et al., 2021). More importantly, since SAR interferograms are not sensitive to image-wide phase biases, there will be no horizontal delay differences over flat terrain. However, for a radar scene with terrain, the differences in the vertical refractivity during both acquisitions will affect phase difference between two arbitrary resolution cells with different topographic height(Hanssen, 2001)(Hanssen, 2001). Therefore, the contribution of tropospheric stratification in the interferogram will only be present if the radar scene has resolution cells with different elevations. So, we compute the differential atmospheric phase delay between location with maximum elevation ($z_{ref} = p$) and all other locations ($z_{ref} = q$) in the radar scene for two SAR acquisition time t_1 and t_2 as:

$$\Delta\emptyset_{atm} = \frac{4\pi}{\lambda cos\theta_{inc}}\left[(L_p^{t_1} - L_q^{t_1}) - (L_p^{t_2} - L_q^{t_2})\right]$$

Then the phase change contribution due to snowpack is estimated as:

$$\Delta\emptyset_s = \Delta\emptyset_{InSAR} - \Delta\emptyset_{atm}$$

43

1070

Tables

Table 1: UAVSAR flight retrieval dates for Grand Mesa during SnowEx'20 campaign.

Flight track	Acquisition Date
3	Feb 01 2020 (02:13:36 – 02:15:58 UTC)
5	Feb 12 2020 (16:47:20 – 16:49:45 UTC)
8	Feb 19 2020 (17:24:18 – 17:27:07 UTC)
13	Feb 26 2020 (17:40:54 – 17:43:34 UTC)
17	Mar 12 2020 (18:17:08 – 18:20:28 UTC)

Table 2: Coherence for treeless and forested environment for different retrievals.

	Period (days)	Coherence (HH)	
		Treeless	Forested
Feb 12-19	7	0.71 ± 0.15	0.65 ± 0.18
Feb 19-26	7	0.6 ± 0.18	0.5 ± 0.2
Feb 1-12	11	0.48 ± 0.18	0.47 ± 0.19
Feb 26 – Mar 12	15	0.49 ± 0.17	0.39 ± 0.18
Feb 1-19	18	0.47 ± 0.18	0.43 ± 0.19
Feb 1-26	25	0.46 ± 0.18	0.43 ± 0.18
Feb 1- Mar 12	40	0.39 ± 0.16	0.36 ± 0.17

Table 3: InSAR retrievals of snow depth change at different polarization for Feb 1-12

Polariation	Coherence	% missing	Avg. Change (cm)
VV	0.51	8	-1.13
HH	0.46	11	-0.1
HV	0.39	36	2.61
VH	0.39	54	-2.67

Table 4: Root mean square error for modeled snow depth (cm) over treeless environments with reference to pit (IOP and TSD) and snow pole measurements.

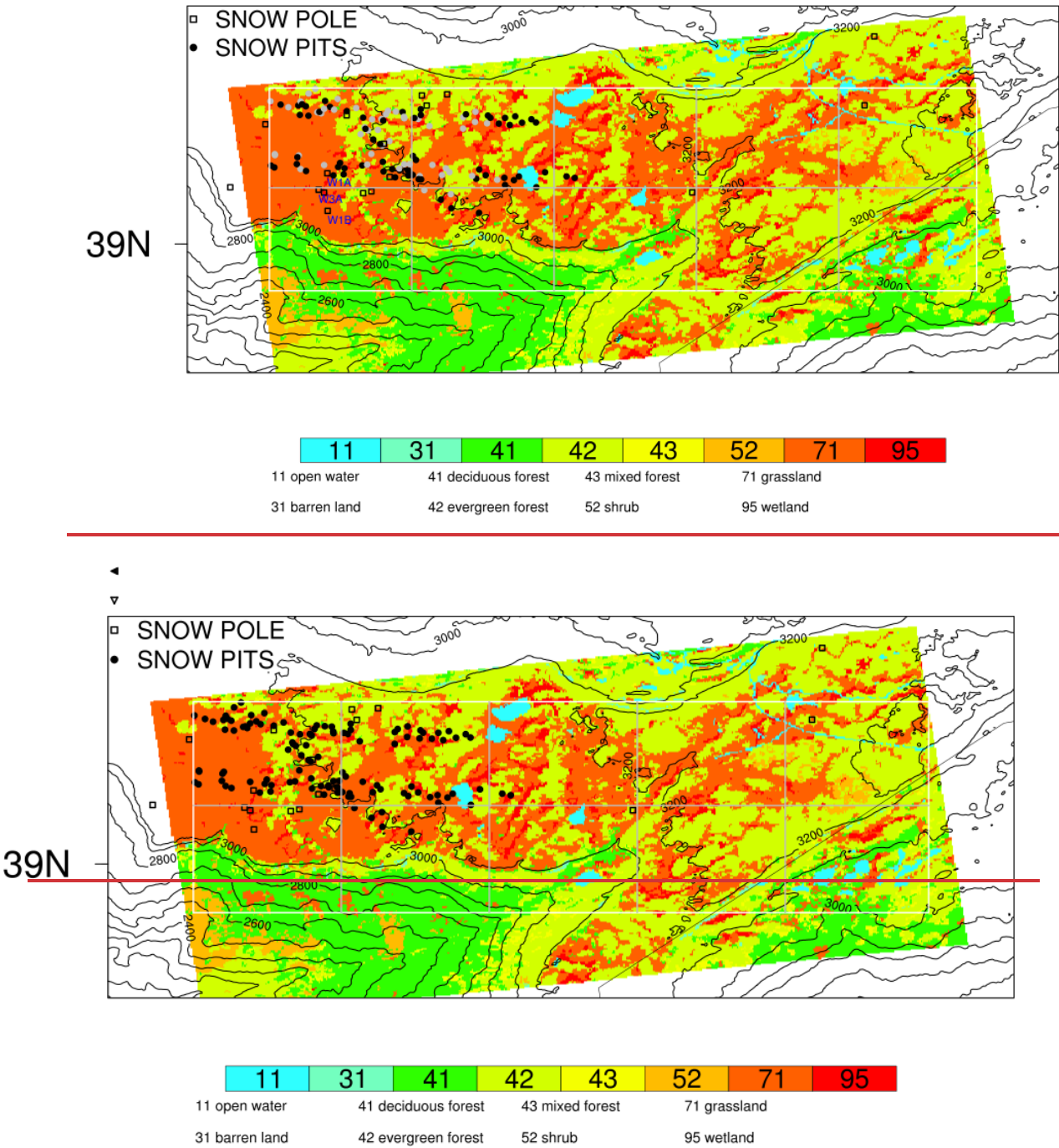|	Pit	W1A	W1B	W3A
CTRL	35.2	17.6	21.2	27.2
OL	36.0	11.57	14.80	30.8
DA	18.3	8.1	21	20.8
DAU	18.0	8.5	22.2	19.2

Figures

Figure 1: Spatial pattern of land cover and topography over the Grand Mesa (GM) domain (white outline). The gray boxes outline the 3 km atmospheric grids. The solid black/gray and square markers show the location of snow pit and snow pole measurements available from SnowEx'20 campaign. The snow pole measurements

1092   used for calibration of InSAR retrievals are also highlighted with their names.
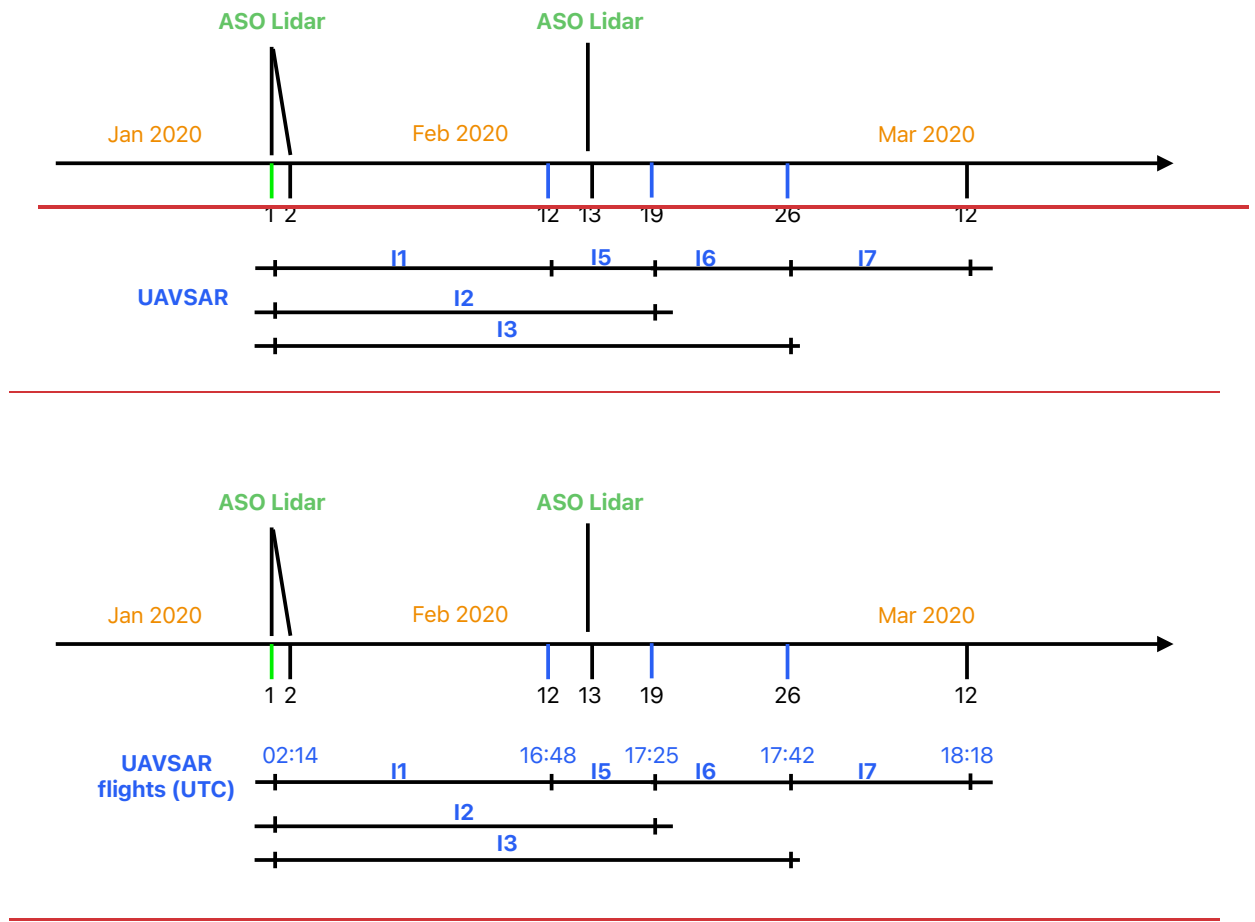
1093

Figure 2: Timeline of availability of UAVSAR interferometric products and ASO Lidar retrievals of snow depth and SWE for SnowEx'20 campaign over Grand Mesa. I1, I2, I3 and I5, I6, I7 indicate the six InSAR pairs used for data assimilation and model evaluation respectively. The dates with green and blue tick mark represent days when the retrievals were used for assimilation in the data assimilation experiments.
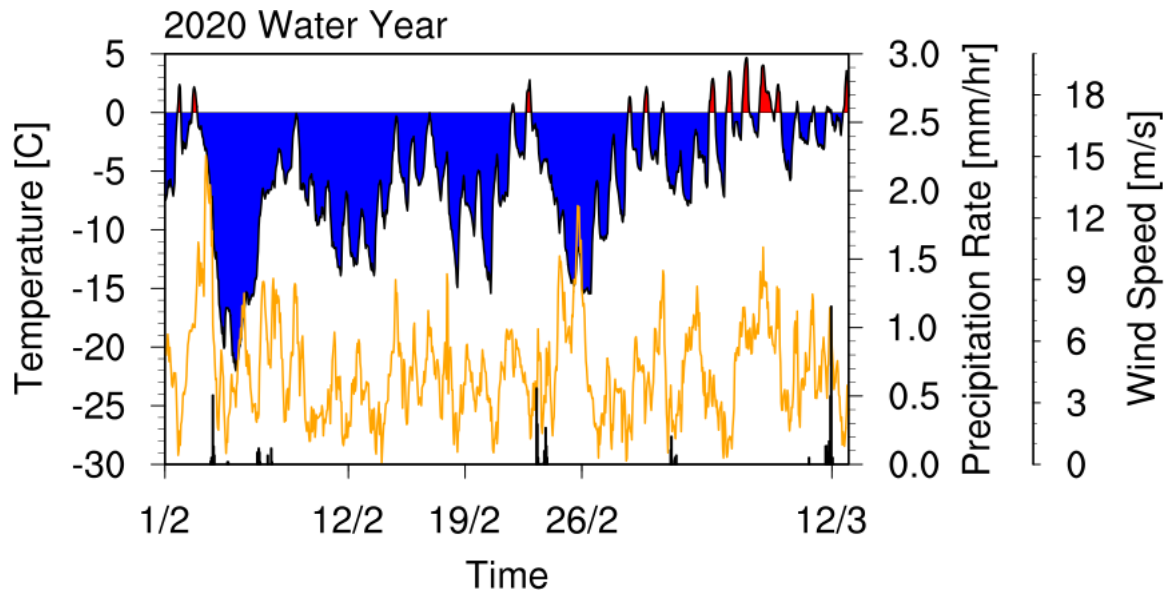
Figure 3: Meteorological data from atmospheric model for north-west GM subdomain showing air temperature (blue/red), wind speed (orange) and precipitation rate (bar plot). The time axis highlights the dates when the L-band UAVSAR flight data were available for SnowEx'20 campaign.

1109

1110
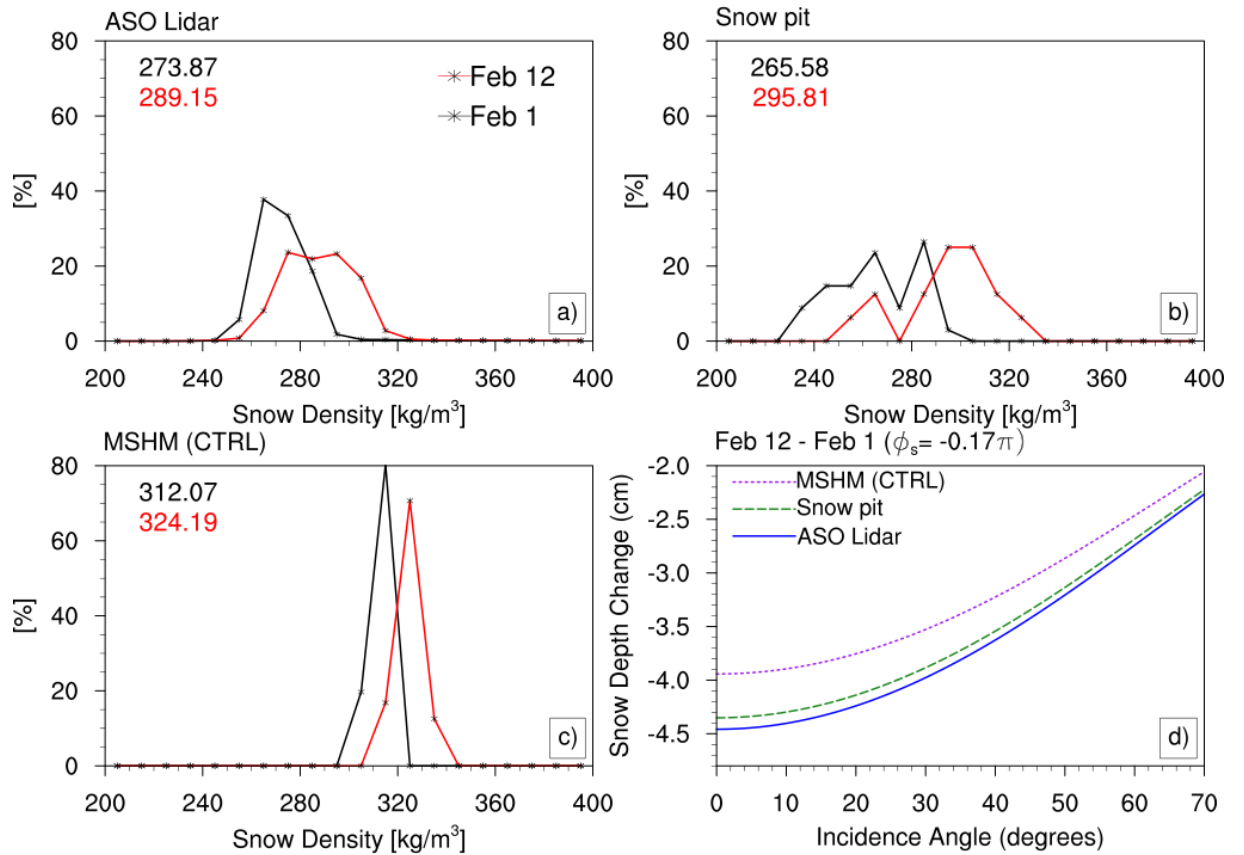
1111 **Figure 4: a-c)** Snow density distribution at two different dates from the ASO Lidar data,

1112 snow pit measurements (Intensive Observation Period, gray solid markers in Fig. 1)

1113 and MSHM control run. **d)** Impact of snow density on the L-band InSAR retrieval of

1114 snow depth change between the two dates as a function of incidence angle for a fixed

1115 change in phase due to snowpack ($\phi_s = 0.17\pi$). The dates for ASO Lidar in actual are

1116 Feb 1/2 and Feb 13. We use Feb 1 and Feb 12, due to availability of InSAR phase data

1117 for these dates.

1118

1119
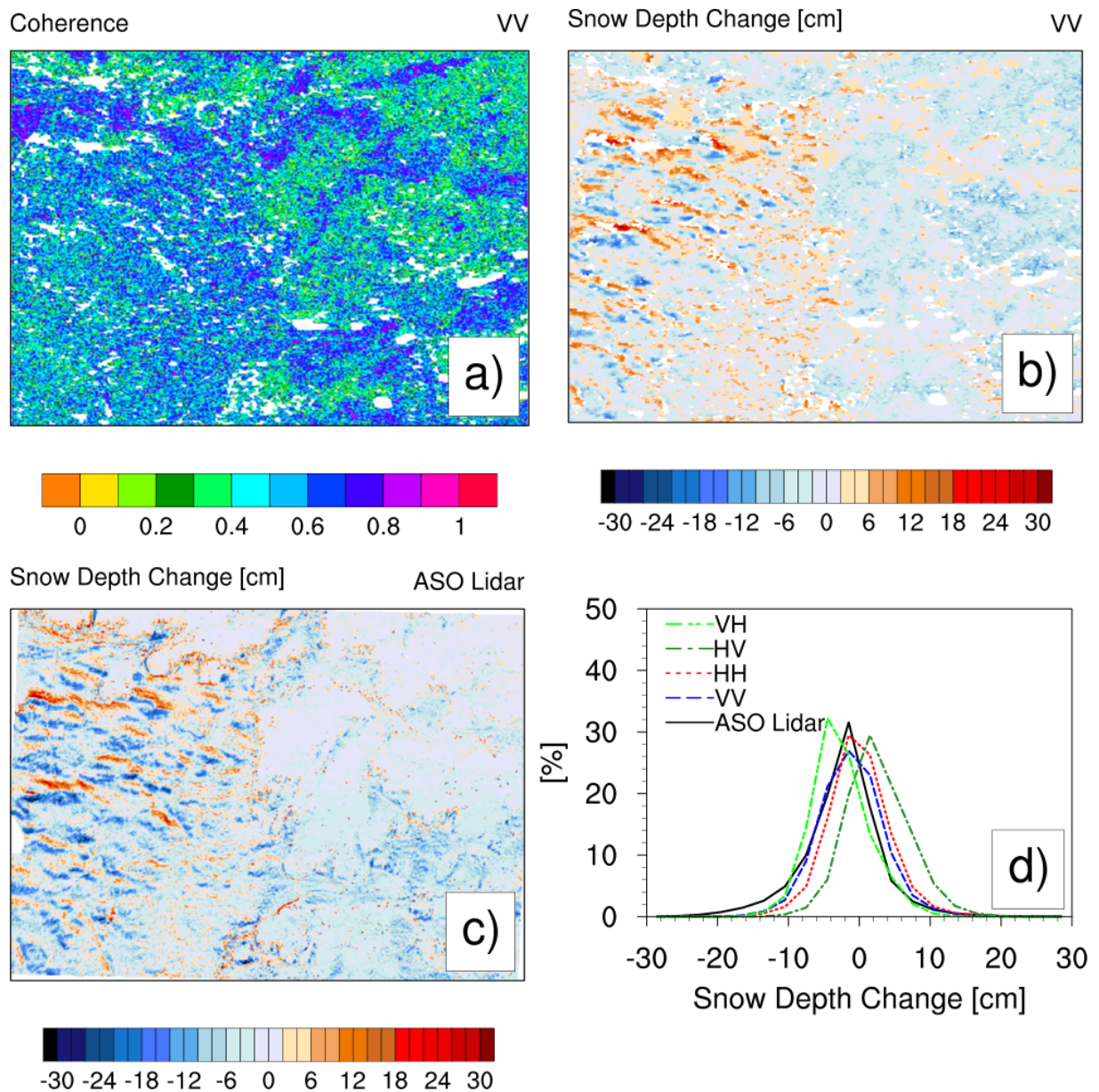
Figure 5: a) Spatial pattern of coherence from L-band VV polarization InSAR retrieval for north-west GM subdomain. **b)** Estimated spatial pattern of snow depth changes from the same retrieval. **c)** Spatial pattern of snow depth change from ASO Lidar data (Feb 1/2–13). **d)** Distribution of change in snow depth for ASO Lidar and InSAR retrievals for VV, HH, HV and VH polarizations. The InSAR retrievals were obtained from UAVSAR flight pairs for Feb 1 and Feb 12.
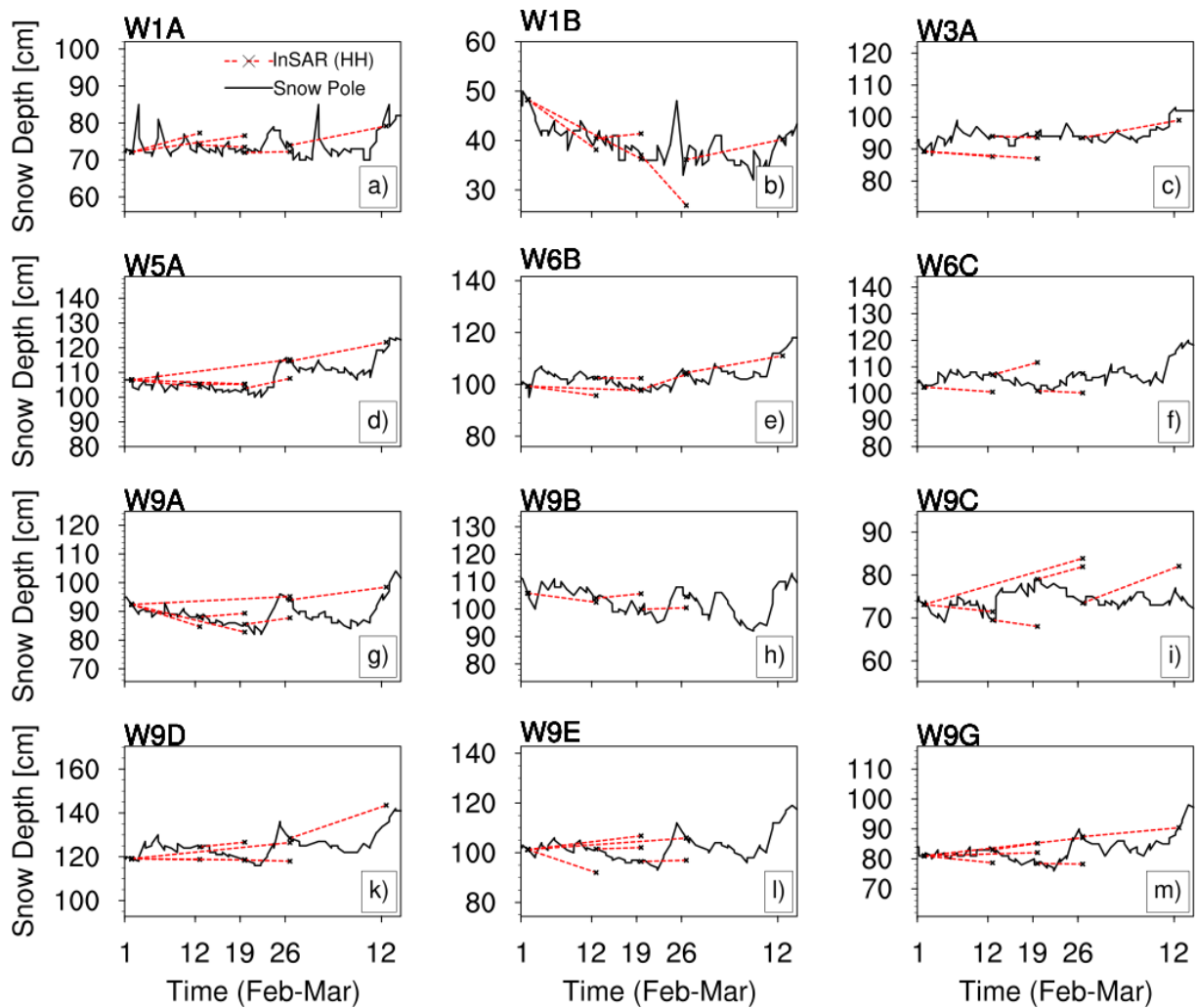
Figure 6: Comparison of L-band InSAR retrieval (HH polarization) of snow depth with Snow Pole measurements for locations with different landcover within the GM domain (**a-c:** Treeless; **d-f:** Sparse trees; **g-m:** Dense trees). For the InSAR retrieval, snow depth measurements from Snow Pole sites were used a reference for the repeat pass UAVSAR flight pairs.
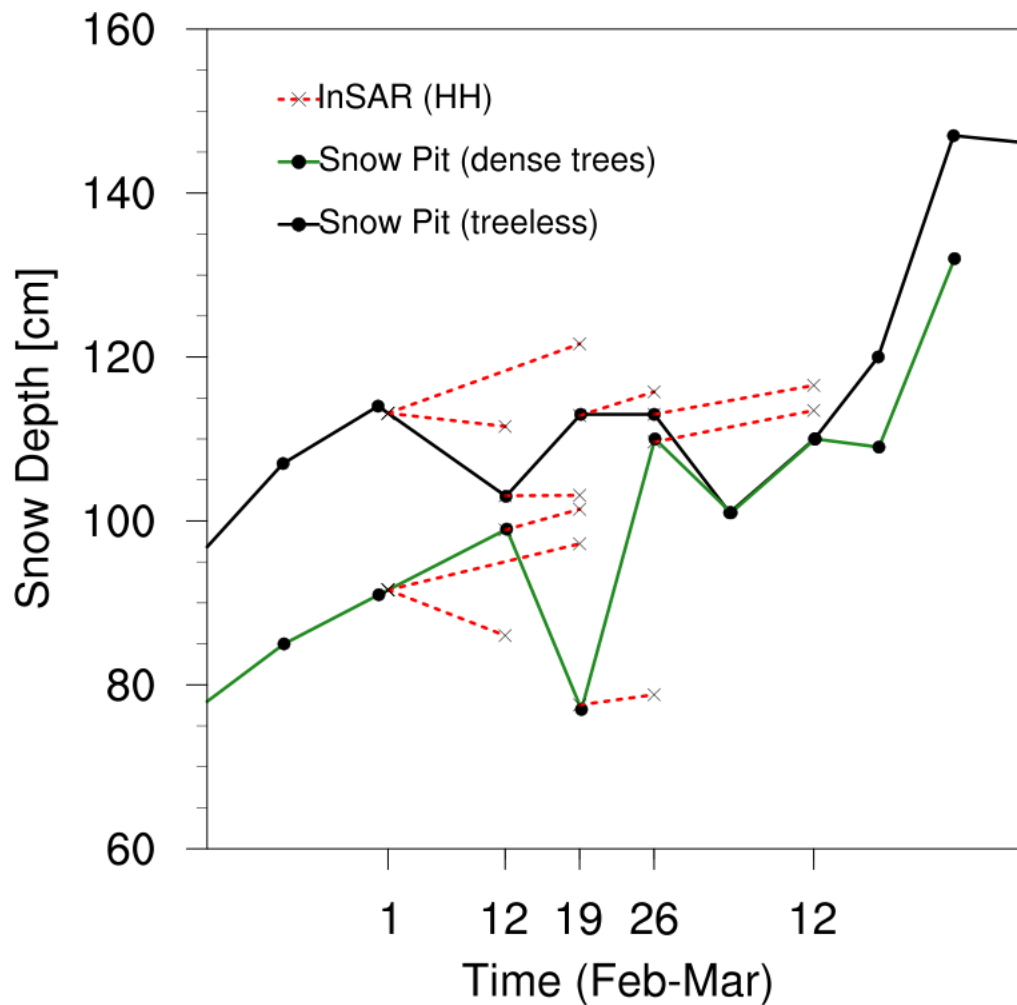
Figure 7: Comparison of L-band InSAR retrieval (HH polarization) of snow depth with snow pit time-series measurements for two locations with different landcover (treeless and dense trees) within the GM domain. For the InSAR retrieval, snow depth measurements from snow pit site were used a reference for the repeat pass UAVSAR flight pairs
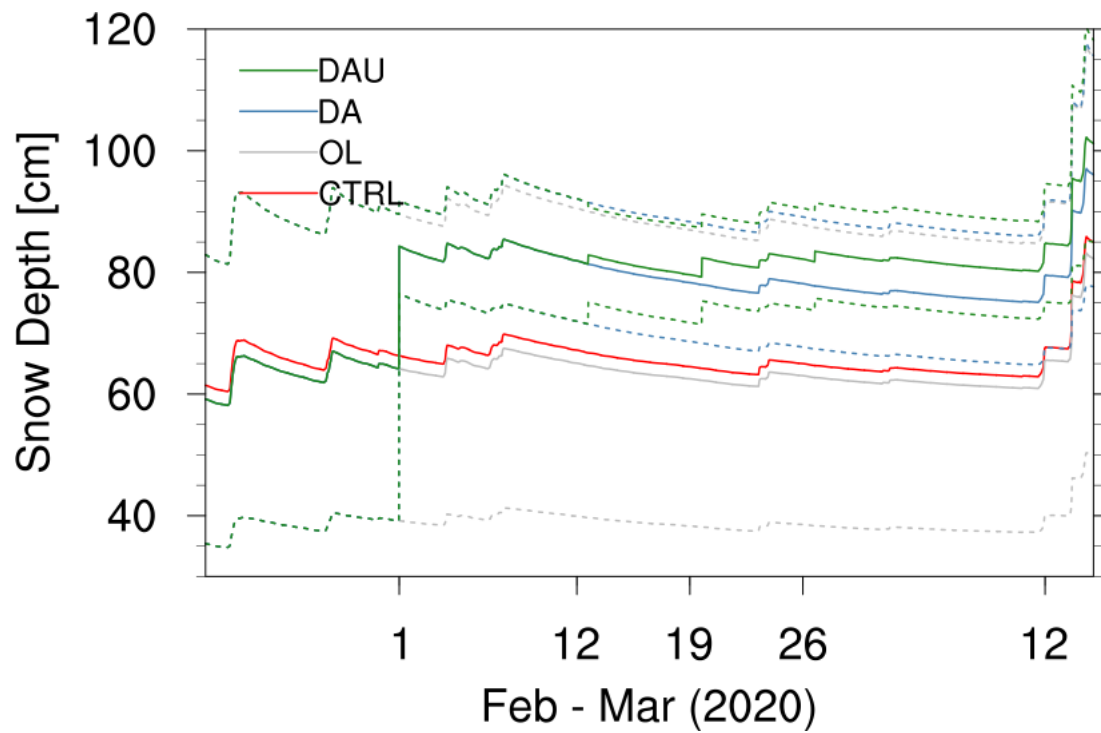
Figure 8: Time series of modeled snow depth for CTRL, OL, DA and DAU run. The dates when observation were assimilated are also shown by tick marks: DA (Feb 1) and DAU (Feb1, Feb 12 and Feb 26) are also shown by the tick marks. The ensemble spread for OL, DA and DAU runs are shown by the dotted lines.
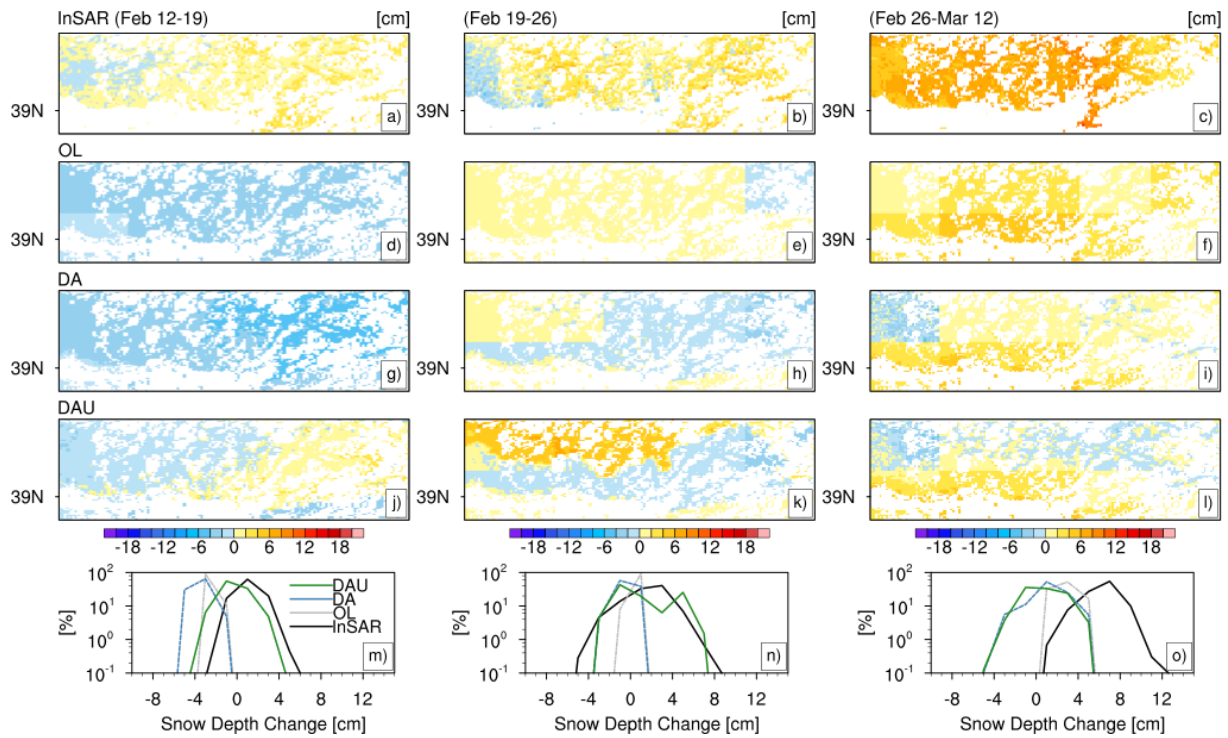
Figure 9: Spatial pattern and histogram of change in snow depth over the GM domain for Feb 12-19, Feb 19-26 and Feb 26-Mar 12: **a-c)** InSAR retrievals, **d-f)** ensemble averaged open loop run (OL), **g-i)** ensemble averaged data assimilation run with ASO Lidar data (DA), **j-l)** ensemble average data assimilation runs with ASO Lidar and referenced InSAR data (DAU), and **m-p)** frequency distribution of snow depth change for InSAR, OL, DA and DAU runs for respective pairs.